RESEARCH ARTICLE

Paraoxonase-2 agonist vutiglabridin promotes autophagy activation and mitochondrial function to alleviate non-alcoholic steatohepatitis

Gu-Choul Shin[1,2] | Hyeong Min Lee[3,4,5] | Nayeon Kim[1] | Jihyeon Hur[3] | Sang-Ku Yoo[5] | Yun Sun Park[5] | Hyung Soon Park[5] | Dongryeol Ryu[6] | Min-Ho Park[7] | Jung Hee Park[7,8] | Sang-Uk Seo[2] | Leo Sungwong Choi[5] | Martin Rønn Madsen[9] | Michael Feigh[9] | Kwang Pyo Kim[3,4] | Kyun-Hwan Kim[1]

[1]Department of Precision Medicine, School of Medicine, Sungkyunkwan University, Suwon, Republic of Korea

[2]Department of Microbiology, College of Medicine, The Catholic University of Korea, Seoul, Republic of Korea

[3]Department of Applied Chemistry, Institute of Natural Science, Global Center for Pharmaceutical Ingredient Materials, Kyung Hee University, Yongin, Republic of Korea

[4]Department of Biomedical Science and Technology, Kyung Hee Medical Science Research Institute, Kyung Hee University, Seoul, Republic of Korea

[5]Glaceum Inc., Suwon, Republic of Korea

[6]Department of Molecular Cell Biology, School of Medicine, Sungkyunkwan University, Suwon, Republic of Korea

[7]Division of Biotechnology, College of Environmental & Bioresource Sciences, Jeonbuk National University, Iksan, Republic of Korea

[8]Advanced Institute of Environment and Bioscience, College of Environmental & Bioresource Sciences, Jeonbuk National University, Iksan, Republic of Korea

[9]Gubra, Hørsholm, Denmark

Correspondence
Kwang Pyo Kim, Department of Applied Chemistry, Institute of Natural Science, Global Center for Pharmaceutical Ingredient Materials, Kyung Hee University, Yongin 446-701, Republic of Korea.
Email: kimkp@khu.ac.kr

Kyun-Hwan Kim, Department of Precision Medicine, School of Medicine, Sungkyunkwan University, Suwon 16419, Republic of Korea.
Email: khkim10@skku.edu

Abstract

Background and Purpose: Only limited therapeutic agents have been developed for non-alcoholic steatohepatitis (NASH). Glabridin, a promising anti-obesity candidate, has only limited druggability due to its low *in vivo* chemical stability and bioavailability. Therefore, we developed vutiglabridin (VUTI), which is based on a glabridin backbone, and investigated its mechanism of action in treating NASH in animal models.

Experimental Approach: Anti-NASH effects of VUTI were determined in *in vitro* fatty liver models, spheroids of primary human hepatocytes and L02 normal liver cell lines. To identify VUTI possible cellular target/s, biotin-labelled VUTI was synthesized and underwent chemical proteomic analysis. Further, the evaluation of VUTI therapeutic efficacy was carried out using an amylin-NASH and high-fat (HF) diet-induced obese (DIO) mouse models. This was carried out using transcriptomic, lipidomic and proteomic analyses of the livers from the amylin-NASH mouse model.

Key Results: VUTI treatment markedly reduces hepatic steatosis, fibrosis and inflammation by promoting lipid catabolism, activating autophagy and improving mitochondrial dysfunction, all of which are hallmarks of effective NASH treatment. The cellular target of VUTI was identified as paraoxonase 2 (PON2), a newly proposed protein target for the treatment of NASH, VUTI enhanced PON2 activity. The results using PON2 knockdown cells demonstrated that PON2 is important for VUTI- activation of autophagy, promoting mitochondrial function, decreasing oxidative stress and alleviating lipid accumulation under lipotoxic condition.

Conclusion and Implications: Our data demonstrated that VUTI is a promising therapeutic for NASH. Targeting PON2 may be important for improving liver function in various immune-metabolic diseases including NASH.

KEYWORDS

autophagy activation, non-alcoholic fatty liver disease, paraoxonase-2, vutiglabridin

1 | INTRODUCTION

Non-alcoholic steatohepatitis (NASH), characterized by hepatic steatosis, inflammation and fibrosis, can progress to hepatic cirrhosis or cancer (Barb et al., 2016). The hepatic accumulation of free fatty acids (FFAs) and toxic lipid intermediates promotes the development of non-alcoholic fatty liver disease (NAFLD) by inducing oxidative stress, mitochondrial dysfunction and hepatic inflammation (Baker & Friedman, 2018). These metabolic disorders, along with the consumption of a high-calorie diet and sedentary lifestyle, are a major public health concern worldwide (Haas et al., 2016). Thus, there is an urgent need to develop therapeutic targets and agents for NASH that can effectively promote toxic lipid metabolite catabolism and mitigate oxidative stress and hepatic inflammation.

Paraoxonase-2 (PON2) is an antioxidant enzyme similar to its more well-known family protein paraoxonases, which prevents oxidative modifications of low-density lipoprotein (Ng et al., 2001). It has been reported that hepatic PON2 activity is decreased in the liver of rats with NAFLD (Hussein et al., 2012). Also, paraoxonase activity was found to be low in patients with biopsy-proven NASH (Kotani et al., 2021). Recently, we showed that the loss of PON2 in hepatocytes leads to imbalanced lipid metabolism, mitochondrial dysfunction, increased oxidative stress and augmented macrophage chemotaxis (Shin et al., 2022), suggesting that impaired PON2 activity in the liver is closely associated with the development and progression of NAFLD. Thus, PON2 may be considered as a potential anti-NASH target.

Glabridin is a potential therapeutic for metabolic diseases, such as obesity and diabetes mellitus (Ahn et al., 2013; Wu et al., 2013). Orally administered glabridin exhibits various beneficial biological activities, including antioxidant, anti-inflammatory and oestrogen-like activities (Belinky et al., 1998; Yehuda et al., 2015). However, the therapeutic effect of glabridin as an anti-NASH agent has not been reported. Glabridin is an important chemical entity in the food, dietary supplement and cosmetic industries (Ao et al., 2010). Despite its various advantages as a potential therapeutic for metabolic diseases, glabridin

---

What is already known

- NASH a common cause of chronic liver disease for which there no effective pharmacological treatment.
- Toxic lipids inactivate paraoxonase-2 thus paraoxonase-2 agonists have been proposed for the treatment for NASH.

What does this study add

- Vutiglabridin (VUTI)-mediated reactivation of PON2 reduces hepatic steatosis, oxidative stress and inflammation.
- VUTI action is related to the PON2-dependent activation of autophagy/mitophagy and promoting mitochondrial function.

What is the clinical significance

- VUTI is a promising therapeutic for non-alcoholic fatty liver diseases.
- Targeting PON2 activity is a valuable approach for the treatment of immune-metabolic diseases (e.g. NASH).

---

has limited applications as a therapeutic drug owing to its low water solubility, bioavailability and chemical stability (Ito et al., 2007). Thus, chemically enhanced derivatives of glabridin should be developed as potential therapeutic agents for immune-metabolic diseases.

We recently synthesized synthetic glabridin derivatives, including vutiglabridin (VUTI) and HSG4113, with improved chemical stability

and oral bioavailability compared with glabridin (Bae et al., 2020). In this study, the therapeutic effect of VUTI on NASH and the mechanism of action of VUTI were elucidated using different mouse models, cell lines and spheroids of primary human hepatocytes (PHHs). We report that VUTI is a PON2 agonist and a promising therapeutic candidate for NASH.

2 | METHODS

2.1 | Animals

All experiments were conducted in compliance with a research protocol approved by the Danish Committee for Animal Research for Jacob Jelsing (2013-15-2934-00784; for amylin [AMLN] diet-induced NASH mouse model) and the Lee Gil Ya Cancer and Diabetes Institute at Gachon University in compliance with the Association for Assessment and Accreditation of Laboratory Animal Care International (AAALAC) standard (Approval No. LCDI-2019-0176; for high-fat diet-induced obese [HF-DIO] mouse model), and the experiments were performed in accordance with their guidelines. Animal studies were also reported in compliance with the ARRIVE guidelines (Percie du Sert et al., 2020) and with the recommendations made by the *British Journal of Pharmacology* (Lilley et al., 2020).

2.1.1 | Amylin diet (AMLN-DIO)-induced NASH mouse model

Male C57BL/6J mice aged 5 weeks (Janvier Labs, France) were housed five animals per cage in a controlled environment (circadian cycle, 12-h light/dark cycle [lights on at 3 AM]; temperature, 21 ± 2°C; humidity, 50% ± 10%). Individual mice were tagged with an implantable microchip (PetID Microchip, E-vet, Haderslev, Denmark). The animals had *ad libitum* access to tap water and the Gubra Amylin NASH diet (AMLN diet) comprising 40% fat (18% trans-fat), 40% carbohydrates (20% fructose) and 2% cholesterol (D09100301, Research Diets, USA). Mice were fed on this diet for 35–37 weeks to establish a severe NASH phenotype. The livers of all mice were biopsied before drug treatment. Following biopsy procedure, animals were single housed. Fibrosis and steatosis stages in the liver biopsies were analysed at baseline (fibrosis score ≥ 1, steatosis score ≥ 2). Individual animals were placed in separate cages. The total number of animals used for each experiment is indicated in the figures and table. An outline of the study design is shown in Fig. S1B and C.

2.1.2 | Liver biopsy in AMLN-DIO NASH mouse model

The liver was biopsied 4 weeks before drug treatment. Briefly, mice were pretreated with enrofloxacin one day before the biopsy. Before the biopsy, mice were anesthetized with isoflurane (2%~3%) in 100% oxygen. A midline abdominal incision was introduced to expose the left

lateral lobe and a cone-shaped liver biopsy sample (50–100 mg) was collected. The sample was fixed in 4% paraformaldehyde overnight and subjected to histological analysis. The cut surfaces were electro-coagulated using an electrosurgical unit (ERBE VIO 100C, ERBE, GA, USA). The liver was returned to the abdominal cavity, the abdominal wall was sutured and the skin was stapled. Mice were intraperitoneally administered with carprofen (5–0.01 mL·kg^{-1} g body weight) at the time of surgery and on days 1 and 2 post-surgery to manage postoperative pain and infection. At week 3 post-biopsy, mice were randomized into various treatment groups based on body weight and liver fibrosis and steatosis scores.

2.1.3 | Drug treatment in the AMLN-DIO NASH mouse model

Mice were orally administered with synthetic glabridin derivatives at doses of 50 and 100 mg·kg^{-1} body weight. One group of mice was subcutaneously administered with semaglutide (30 nmol·kg^{-1} body weight) once daily. Drug treatment and diet were continued for 6 weeks (for experiments comparing the effects of VUTI and HSG4113) or 10 weeks (for experiments comparing the effects of semaglutide and VUTI). Food intake was measured once daily for 2 weeks after the initiation of drug treatment. The blood samples were collected from the tail vein of mice under fasting conditions five days before the end of the experiment to determine the blood glucose and insulin levels. Additionally, a terminal blood sample was collected from the tail vein of non-fasting mice for plasma biochemical analysis. Mice were killed by cardiac puncture under isoflurane anaesthesia. The liver samples were excised, weighed and processed for further analysis.

2.1.4 | High fat diet-induced obese (HFDIO) mouse model

Male C57BL/6J mice aged 14 weeks (Jackson Labs, USA) were housed five animals per cage and fed a high-fat (60% trans-fat) (D12492, Research Diets, USA) or normal diet (10% trans-fat; Picl-Lab5053, LabDiet, USA) starting at 6 weeks of age in clean cage with water bottle and saw dust bedding. Mice were randomly divided into groups such that the mean body weights of the obese groups were equal. Then, the animals had two weeks of administration adaptation period before dosing. At 17 weeks of age, the animals were dosed orally via gastric intubation (50 or 100 mg·kg^{-1}) for vutiglabridin (VUTI) or subcutaneously via insulin syringe (5 mL·kg^{-1}) for semaglutide once a day for 6 weeks. Following first drug treatment, animals were single housed. At the end of the study, animals were fasted for 14–16 h and killed by an overdose isoflurane anaesthetic.

2.2 | Body weight and body composition analysis

Body weight was monitored daily during the treatment period. Whole-body fat and lean mass were analysed during the 10 weeks of

treatment using non-invasive EchoMRI scanning with EchoMRI-900 (EchoMRI, TX, USA). During the scanning procedure, mice were placed in a restrainer for 90–120s. To analyse the body composition parameters at the end of the study period, the weights of the liver, epididymal white adipose tissue (EWAT), peri-renal white adipose tissue and gastrocnemius muscle were determined.

Biochemical analysis: the abdominal cavity of the AMLN-DIO NASH mice was opened under non-recovery isoflurane anaesthesia and the cardiac blood sample was collected using a syringe. The blood sample was transferred into a microvette/vacuette containing an anticoagulant, mixed five times by inversion, and stored at 4°C until centrifugation. The plasma samples (supernatant) were transferred to new tubes and immediately frozen on dry ice and stored at −80°C until use. The Fgf21, Tnf, Il10, Il15, Il6, and Cxcl1 levels in the plasma were measured in duplicates using an enzyme-linked immunosorbent assay kit (BioVendor) following the manufacturer's instructions. The levels of leptin and insulin were measured using the MSD platform (Meso Scale Diagnostics) following the manufacturer's instructions.

Tail blood (≤ 200 μL) at the end of the experiment of the HFDIO mice was pressed into an open microvette (200 μL) containing an appropriate anticoagulant. The blood samples were stored at 4°C until centrifugation. The plasma was separated, transferred to new tubes, immediately frozen on dry ice, and stored at −80°C until use. HDL, LDL, TC, ALT, AST and ALP levels were measured using commercial kits (Roche Diagnostics) with the Cobas c501 autoanalyzer following the manufacturer's instructions. For evaluation of blood glucose levels at five days before the end of the experiment in the AMLN-DIO NASH mouse model, mice were restrained using the mechanical restraint device and the tail blood samples were collected into heparinized glass capillary tubes and immediately suspended in glucose/lactate system solution buffer (EKF-Diagnostics, Germany). Next, the blood glucose levels were measured using a BIOSEN c-Line glucose meter (EKF-Diagnostics) following the manufacturer's instructions. To analyse insulin levels, the blood samples were collected in heparinized tubes, and the plasma was separated and stored at −80°C until use. The insulin levels were measured using the MSD platform (Meso Scale Diagnostics) following the manufacturer's instructions. For liver cholesterol and triacylglycerol (TAG) analysis, the liver samples were homogenized and heated twice at 90°C in 5% NP-40 to extract triacylglycerol and cholesterol. The samples were centrifuged, and the triacylglycerol and cholesterol content in the supernatant was measured using commercial kits (Roche Diagnostics) with the Cobas c501 autoanalyzer following the manufacturer's instructions. Hepatic oxidative stress was assessed using the thiobarbituric acid reactive substance assay.

2.3 | Histological analyses

Biopsy samples obtained at the baseline and end of the study period (both from the left lateral lobe) were fixed overnight in 4% paraformaldehyde. The liver tissue was paraffin-embedded and sectioned (3-μm thickness). The sections were stained with H&E and anti-

galectin 3 (LGLAS3), anti-actin alpha 2 (ACTA2) , anti-adhesion G protein-coupled receptor E1 (ADGRE1), anti-microtubule-associated proteins 1A/1B light chain 3B (MAP1LC3B/LC3B) and anti-beclin 1 (BECN1) antibodies following the manufacturer's instructions. The samples were subjected to quantitative histomorphometry using Visiomorph digital imaging software (Visiopharm, Hørsholm, Denmark) or NIH ImageJ software (http://rsbweb.nih.gov/ij/). The primary antibodies used in this study are listed in Supplementary Table 3. The fractional area of liver fat accumulation (macrosteatosis) was determined using HE-stained sections and expressed as a percentage of the total sectional area. Hepatic lipid droplet accumulation, which indicates hepatic steatosis, was confirmed using oil red O staining. Liver fibrosis was examined using picrosirius red staining. The Lgals3-positive and Acta2-positive areas were expressed as a percentage of the total parenchymal area by subtracting the corresponding fat area determined on adjacent HE-stained sections. Macrophage infiltration in the liver was assessed based on Adgre1 immunostaining and Ccl2 expression. Autophagy activation in the liver was determined based on Map1lc3b and Becn1 immunostaining. The staining intensities of Map1lc3b/Lc3b and Becn1 are represented as inverted median pixel value (IMPV).

To examine adiposity, the paraffin-embedded EWAT sections were subjected to H&E staining. The average adipocyte size in EWAT was measured using morphometry with NIH ImageJ software. All histological assessments were performed by experienced histologists blinded to the experimental groups. Steatosis, lobular inflammation, hepatocyte ballooning and fibrosis in the liver were scored before and after treatment using the NASH activity score (NAS) and fibrosis staging system.

2.4 | Analysis of hepatic inflammation and mitochondrial function

Inflammation in the liver was determined based on immunoblotting to Il1b and Tnf. Mitochondrial metabolic capacity in the liver was determined based on immunoblotting to phospho-Prkaa, Prkaa, Ppargc1a, and OXPHOS component (Atp5a, Uqcrc2, Mtco1, Sdhb and Ndufb8). To mitochondrial DNA content, genomic DNA and mitochondrial DNA were extracted from the liver tissues using DNeasy kit (Qiagen) following the manufacturer's instructions. Briefly, 2.5 ng DNA were used to quantify the mitochondrial DNA and normalized with the genomic DNA using mitochondrial mt-Nd1 primers (Forward: GTGACGTTGACATCCGTAAAGA; Reverse: GTAACAGTCCGCCTAGAAGCA C) and nuclear Pecam1 primers (Forward: ATGGAAAGCCTGCCATCATG; Reverse: TCCTTGTTGTTCAGCATCAC).

2.5 | RNAseq and data analysis in the AMLN-DIO NASH mouse model

The liver samples after treatment (15 mg fresh tissue) and gastrocnemius muscle were subjected to RNAseq. The RNA quantity and

quality were measured using Qubit (Thermo Fisher Scientific, OR, USA) and a bioanalyzer with RNA 6000 Nano kit (Agilent, Waldbronn, Germany), respectively. RNA sequence libraries were prepared using NeoPrep (Illumina, CA, USA) with Illumina TruSeq stranded mRNA Library kit for NeoPrep (Illumina) and sequenced on NextSeq 500 (Illumina) with NSQ 500 hi-Output KT v2 (75 CTS, Illumina). The sequencing reads were aligned to the GRCm38 v84 Ensembl Mus musculus genome using STAR v.2.5.2a with default parameters. Differential gene expression analysis was performed with DEseq2. The difference in the expression of genes with a Benjamini-Hochberg-adjusted P value of ≤ 0.05 (5% false discovery rate (FDR)) was considered significant.

2.5.1 | Protein extraction and digestion

cryo-pulverized liver tissues (wet weight: 40–50 mg) were homogenized in 1 mL radioimmunoprecipitation assay (RIPA) lysis buffer (Pierce) (5% sodium dodecyl sulfate [SDS], 0.1 M Tris-HCl [pH 7.6], $1\times$ Halt protease inhibitor [Pierce], and $1\times$ phosphatase inhibitor [PhosSTOP, Roche]). The lysates were centrifuged at 20,000 $\times$g for 10 min, and the supernatant was transferred to a new tube. The protein concentration in the supernatant was measured using the bicinchoninic acid (BCA) protein assay kit (Pierce). Protein samples (600 μg) were divided into two equal portions, and each portion was digested separately using an S-Trap method (Katelyn et al., 2018). Briefly, 300 μg of proteins were incubated with 20 mM dithiothreitol (DTT) for 10 min at 95°C on a thermomixer (Thermo Fisher Scientific). The proteins were then alkylated with 50 mM iodoacetamide for 30 min in the dark. Before digestion, phosphoric acid at a final concentration of 1.2% and six volumes of binding buffer (90% methanol; 100 mM triethylammonium bicarbonate [TEAB]; pH 7.1) were added to the sample and gently mixed. The protein solution was loaded onto an S-Trap filter and centrifuged at 3000 rpm for 1 min. The flow-through was collected and reloaded onto a filter. This step was repeated thrice. The filter was washed thrice with 300 μL of binding buffer. Digestion was performed with Lys-C (Pierce) for 1 h and trypsin (Pierce) overnight (enzyme-to-protein ratio = 1:50). The peptides were eluted twice using the following three buffers (200 μL each): 50 mM TEAB, 0.2% formic acid in H_2O, and 50% acetonitrile and 0.2% formic acid in H_2O.

2.5.2 | Tandem mass tag (TMT)-16 labelling and peptide fractionation

Eluted peptides (400 μg) from each sample were labelled with 16-plex TMT reagents (Thermo Fisher Scientific, Germany) following the manufacturer's instructions. The peptides were solubilized in 100 μL of 100 mM TEAB (pH 8.5) solution and incubated with the labelling reagent in 20 μL of acetonitrile for 1 h with shaking. To quench the unreacted TMT reagents, 8 μL of 5% hydroxylamine was added. Differentially labelled peptides were then mixed (16×400 μg) and dried using a vacuum centrifuge. The quenched, combined sample was

desalted using a C18 column (Harvard apparatus). The pooled TMT-labeled peptide sample was fractionated using basic pH reverse-phase liquid chromatography with an Agilent 1260 Infinity HPLC system (Agilent, CA, USA). The chromatography conditions were as follows:- column, Xbridge C18 analytical column (4.6 mm × 250 mm); solvent A, 10 mM ammonium formate in water (pH 9.5); solvent B, 10 mM ammonium formate in 90 % acetonitrile (pH 9.5); gradient time, 105 min; flow rate, 500 mL/min. The gradient conditions were follows: 0% solvent B for 10 min; 0%–13% solvent B for 10 min; 13%–40% solvent B for 60 min; 40%–70% solvent B for 15 min; 70% solvent B for 10 min; 70%–0% solvent B for 10 min. In total, 96 fractions were collected every minute from 15 to 110 min. The fractions were pooled into 24 non-contiguously concatenated peptide fractions. The resultant 24 fractions were dried and stored at −80°C.

2.5.3 | Phosphopeptide enrichment

The phosphopeptides from 12 fractions obtained by combining sequential fractions of the 24 fractions (e.g. F1 and F2 or F3 and F4) were enriched using immobilized metal affinity chromatography (IMAC). IMAC beads were prepared from Ni-nitrilotriacetic acid (NTA) magnetic agarose beads. Ni-NTA beads (500 mL) were washed thrice with water. The beads were then incubated with 100 mM EDTA (pH 8.0) for 30 min with end-over-end rotation to remove nickel ions. The EDTA solution was removed, and the beads were washed thrice with water. The NTA beads were treated with 10 mM of aqueous FeCl3 solution for 30 min with end-over-end rotation. Iron-chelated IMAC beads were washed thrice with water. Ni-NTA agarose beads were used to prepare Fe^{3+}-NTA agarose beads. Approximately 300 μg of peptides from each phosphor-proteome fraction were reconstituted in 500 μL of 80% MeCN/0.1% trifluoroacetic acid (TFA). The solution was incubated with IMAC beads for 30 min on a shaker at room temperature. The samples were briefly centrifuged using a tabletop centrifuge. The clarified peptide flow-throughs were separated from the beads, and the beads were reconstituted in 200 mL IMAC binding/wash buffer (80 MeCN/0.1% TFA) and loaded onto equilibrated Empore C18 silica-packed stage tips (3M, 2315). The samples were then washed twice with 50 μL of IMAC binding/ wash buffer and once with 50 μL of 1% FA and eluted thrice from the IMAC beads to the stage tips with 70 μL of 500 mM dibasic sodium phosphate (pH 7.0). The stage tips were then washed once with 100 mL 1% FA. Phosphopeptides were eluted from the stage tips with 60 μL of 50% MeCN/0.1% FA.

2.5.4 | LC-ESI-MS/MS analysis of the proteome

All peptide samples were separated using an ultra-performance liquid chromatography system equipped with analytical columns (75 μm × 50 cm, C18, 3 μm, 100 Å) and trap columns (75 μm × 2 cm, C18, 3 μm, 100 Å). The mobile phases were as follows: solvent A, 0.1% formic acid in water; solvent B, 0.1% formic acid in 90% acetonitrile. The solvent gradient conditions for global proteome profiling analysis were

as follows:-2% solvent B for 8 min, 2%–10% solvent B for 3 min, 10%–25% solvent B for 113 min, 25%–40% solvent B for 20 min, 70% solvent B for 4 min, and 2% solvent B for 20 min. Meanwhile, the gradient conditions for phosphoproteome analysis were as follows:- 2% solvent B for 8 min, 2%–10% solvent B for 3 min, 10%–20% solvent B for 123 min, 20%–30% solvent B for 20 min, 70% solvent B for 4 min, and 2% solvent B for 20 min. For global peptide analysis, 2 µg of peptides from each of the 24 fractions were individually analysed. All enriched peptides from each of the 12 fractions were injected for phosphopeptide analysis. The eluted peptides from LC were analysed using a Q Exactive plus orbitrap mass spectrometer (Thermo Fisher Scientific) equipped with an easy-spray nano source. Data acquisition was performed using Xcalibur Q Exactive v2.1 software in positive ion mode at a spray voltage of 2.0 kV. MS1 spectra were captured under the following conditions: resolution, 70,000; AGC target, 1e6; mass range, 400–1800 m/z; mode cycle time, 2 s. MS2 spectra were captured under the following conditions: resolution, 35,000; AGC target, 2e5; isolation window, 2.0 m/z; maximum injection time, 100 ms; HCD collision energy, 32%. The peptide mode was selected for monoisotopic peak determination. Charge state screening was enabled to only include precursor charge states 2–6, with an intensity threshold of 5e4. Peptides that triggered MS/MS scans were dynamically excluded from further MS/MS scans for 30 s, with a mass tolerance of 10 ppm (±).

2.5.5 | Protein and phosphopeptide identification

The acquired raw files were processed using Proteome Discoverer v.2.4 (Thermo Fisher Scientific) software environment with the built-in Sequest HT search engine for the identification of peptides and phosphopeptides. The data were searched using a target-decoy approach against Uniprot Human (Jan 2021, 20,452 entries) reference proteome (FASTA file) (FDR < 1%) at the level of proteins, peptides, and modifications, using minor changes to the default settings as follows: -oxidized methionine (M); in case of phosphopeptides, search phospho (S,T,Y) was selected as variable modifications, while carbamidomethyl (C) selected as fixed modification. A maximum of two missed cleavages and a minimum peptide length of seven amino acids were allowed. Enzyme specificity was set to trypsin. An initial precursor mass deviation up to 10 ppm and a fragment mass deviation up to 0.06 Da were allowed. To quantify each reporter ion in the sample, 'reporter ion quantifier' with TMT 16-plex was used. For highly confident quantifications of protein, the protein ratios were calculated from two or more unique quantitative peptides in each replicate. All reporter ion intensities were transformed to log2 values. Proteins that did not display all values in at least one group were filtered out

2.5.6 | Proteomic data analysis

For global proteome analysis, the tandem mass tag (TMT) intensities of the peptides were normalized using the quantile normalization method. Differentially expressed proteins (DEPs) were identified using an integrative statistical method. Briefly, log2 (intensity) of each protein was applied to its abundance for all replicates. The fold change and adjusted P value were calculated using Student's t test. Finally, DEPs with a combined fold change value of 1.5 and a P value < 0.05 were selected. The same normalization and statistical method was used for phosphoproteome analysis. Differentially phosphorylated peptides (DPPs) that were uniquely assigned to the protein were selected. To explore the signal pathway in which the DEPs and DPPs are enriched, Kyoto Encyclopaedia of Genes and Genomes (KEGG) enrichment and Reactome pathway analyses were performed using the g:Profiler. To reconstruct drug-related network modelling, protein-protein interactions (PPIs) were obtained from the STRING database. Network models were developed for a list of selected proteins for network analysis based on the collected PPIs. In the network models, the nodes were arranged based on the KEGG and Reactome Pathway database analyses.

2.6 | Lipidomics in AMLN-DIO NASH mouse model

2.6.1 | Lipid extraction

Liver samples were weighed and individually cryo-pulverized using a Cryoprep device (CP02, Covaris). The lyophilized samples from each tissue were aliquoted to separate tubes (50 mg for proteomic analysis and 20 mg for lipidomic analysis) and stored at −80°C. For lipid analysis of liver tissues, a two- step lipid extraction method was performed. To perform the neutral extraction, liver tissues were thawed on ice and incubated with internal standards (10 µL) and methanol/chloroform (2:1 (v/v); 990 µL). The samples were vortexed for 60 s. The standard mix SPLASH Lipidomix Mass Spec Standard j 330707 supplemented with LPG (14:0), LPI (13:0), LPA (14:0), ceramide (d18:1−12:0), So (d17:1), Sa (d17:0), ceramide P (d18:1−12:0), So1P (d17:1), Sa1P (d17:0) and free fatty acids (FFA, 20:4-d8) was used. The sample was incubated for 10 min on ice and centrifuged at 15,000 ×g and 4°C for 2 min. Next, 950 µL of the supernatant was transferred to a new tube. To perform the acidic extraction, the remaining tissue was incubated with 750 µL of chloroform/methanol/37% HCl (40:80:1 v/v/v) mixture for 15 min at room temperature. Next, 250 µL of cold chloroform and 450 µL of cold 0.1 N HCl were added to the sample. The samples were vortexed for 1 min and centrifuged at 7000 ×g and 4°C for 2 min. The bottom organic phase was collected, pooled with a prior extract, and dried using a SpeedVac concentrator.

2.6.2 | Lipid measurement using LC-MS

HPLC-ESI-MS/MS analyses were performed using a 1200 series HPLC system (Agilent Technologies, DE, USA) coupled with a 6490 Accurate-Mass Triple Quadrupole Mass Spectrometer (Agilent

Technologies). The LC-MS/MS conditions were as follows: column, Hypersil GOLD column (2.1 × 100 mm ID; 1.9 μm, Thermo Fisher Scientific); solvent A (acetonitrile/methanol/water (19:19:2 v/v/v) + 20 mmol/L ammonium formate + 0.1% (v/v) formic acid); solvent B, (2-propanol +20 mmol/L ammonium formate + 0.1% (v/v) formic acid); flow rate, 250 μL·min^{-1}; total run time, 33 min; sample injection volume, 5 μL. The gradient elution program was as follows: 0–5 min, solvent B 3%; 5–18 min, solvent B 5–30%; 18–24 min, solvent B 30%–90%; 24–28 min, solvent B 90%; 28–29 min, 90%–3%; and 29–33 min, solvent B 3%. The parameters of operating source conditions were as follows:- capillary voltage in positive mode, 3500 V; capillary voltage in negative mode, 3000 V; sheath gas flow rate, 11 L/min (UHP nitrogen); sheath gas temperature, 200°C; drying gas flow rate, 15 L/min; drying gas temperature, 150°C; nebulizer gas pressure, 25 psi. The optimal dMRM conditions were used to analyse various lipid species.

2.6.3 | Lipidomics data analysis

Agilent Mass Hunter Workstation Data Acquisition software was used to process the LC/MS data. Qualitative Analysis B.06.00 software (Agilent Technologies) was used to export the m/z of precursor and product ions and retention time of target lipids in the multiple reaction monitoring data. The area of the assigned peak in the raw data was calculated using an in-house database constructed using the Skyline software package (MacCoss Laboratory, University of Washington, WA, USA). Lipid abundance was normalized to tissue weight and internal standard peak area. MetaboAnalyst Web site (https://metaboanalyst.ca) was used to perform PCA and projection to latent structure discriminant analysis (PLS-DA). Unweighted correlation network graphs were generated based on Spearman's correlation. All nodes with P values less than 0.05 were used in SPSS version 21.0 (IBM Corp, NY, USA). Heatmaps were generated using the Morpheus website (https://software.broadinstitute.org/morpheus).

2.7 | Cell culture and cytotoxicity assay

L02 cells (an immortalized normal liver cell line, RRID:CVCL_6926) were a kind gift from Dr. KH Lee (Korea Institute of Radiological and Medical Sciences). The cells were cultured in Dulbecco's modified Eagle's medium (DMEM) (Welgene, LM001-05) supplemented with 10% foetal bovine serum (FBS) and 100 U·ml^{-1} of penicillin and streptomycin at 37°C in a 5% CO_2 incubator.

For cytotoxicity analysis in L02 cells, cells were seeded into a 96-well culture plate and were treated with a different concentration of VUTI (2.5, 5, 10, 25 and 50 μM) for 24 h, and MTT (3-(4, 5-dimethylthiazolyl-2)-2, 5-diphenyltetrazolium bromide) solution (5 mg·ml^{-1} of the final concentration) was treated for 2 h. The supernatant was removed from the well, and the precipitate obtained was dissolved in DMSO. The levels of insoluble formazan formation were determined at 570 nm using a SpectraMax Plus 384 Microplate Reader (Agilent Technologies, Seoul, Republic of Korea).

2.8 | Generation of PON2 knockdown cells and mt-Keima cells

Stable PON2 knockdown (KD) L02 cells were generated by transducing the cells with a recombinant lentivirus vector harbouring a short hairpin RNA against PON2 (shPON2; Genecopoeia, LPP-HSH013480-LVRU6P). PON2 KD cells were cultured in DMEM supplemented with puromycin (500 ng·ml^{-1}) (Life Technologies, A11138-03). The KD of PON2 was confirmed using immunoblotting with anti-PON2 antibodies.

Cells stably expressing mt-Keima were generated by transducing the cells with a recombinant lentivirus vector containing the mt-Keima cDNA for 48 h. The recombinant cells were selected with puromycin (500 ng·ml^{-1}). The packaging vectors pSPAX2 and pMD2.0G were co-transfected with pmt-Keima into HEK293T cells for 72 h. The cell supernatant was filtered through a 0.22-μm membrane filter. The virus was concentrated by subjecting the samples to ultra-centrifugation at 45,000 × g. The supernatant was discarded, and the viruses were suspended in an appropriate amount of phosphate-buffered saline (PBS) and stored at −80°C until use.

To prepare the BSA-conjugated palmitic acid, a 100-mM palmitic acid solution was prepared in 0.1-mM NaOH and heated at 70°C. Palmitic acid solution was incubated with 10% BSA at 55°C for 30 min to obtain 5-mM palmitic/1% BSA. The solution was then cooled to 25°C, filter-sterilized and stored at −20°C until use. The cells were incubated with a culture medium containing 400-μM FFA (150-μM BSA-conjugated oleic acid and 250-μM BSA-conjugated palmitic acid) in the presence or absence of 3-μM VUTI.

2.9 | 3D spheroid culture of primary human hepatocytes (PHHs)

Spheroid-qualified human primary hepatocytes (Thermo Fisher Scientific, HMCPSQ) were thawed according to the manufacturer's instructions and seeded in ultra-low attachment plates (Corning, CLS7007) at a density of 2000 viable cells per well. Cells were seeded in William's E medium (Thermo Fisher Scientific, A1217601) supplemented with dexamethasone (Thermo Fisher Scientific, A13449) and primary hepatocyte thawing and plating supplements (Thermo Fisher Scientific, CM3000). After spheroid aggregation on Day 3 after seeding, spheroids were further cultured in William's E medium supplemented with dexamethasone, GlutaMAX supplement (Thermo Fisher Scientific, 35050061), penicillin–streptomycin (Thermo Fisher Scientific, 15140148) and insulin–transferrin–selenium (Thermo Fisher Scientific, 41400045).

2.10 | Lipid accumulation assay

For the 2D culture system, cells were plated in six-well plates and incubated with 400-μM FFA in the presence or absence of 3-μM VUTI for 72 h. The cells fixed with 4% paraformaldehyde for 10 min were stained with Oil Red O solution for 15 min at room temperature.

After washing once with 60% isopropanol, the cells were rinsed with distilled water. The images were captured using an inverted microscope (Carl Zeiss Axio Imager M2 fluorescence microscopy). The signal intensity was analysed using the National Institutes of Health (NIH) ImageJ software.

For the 3D spheroid culture system, exposure and treatment with 400-μM FFA in the presence or absence of 1- to 5-μM VUTI started on Day 3 after seeding of primary human hepatocyte, which hereafter is referred to as Day 0. Spheroids were administered every 48–72 h with FFA and VUTI and fixed with 4% paraformaldehyde on Day 7 after treatment with FFA and VUTI. Spheroids were stained with 2-μM Nile Red (Sigma-Aldrich, 72485) in PBS, together with 1-μg·ml^{-1} Hoechst 33342 (Thermo Fisher Scientific, H3570), for 15 min at room temperature. Spheroids were washed thrice with PBS. The images were captured using a Carl Zeiss Confocal LSM710 Meta microscope and processed using the software supplied by the manufacturer (Carl Zeiss, Seoul, Republic of Korea). The intensity of neutral lipid staining was quantified and normalized for the number of nuclei per spheroid using the NIH ImageJ software.

2.11 | Autophagy flux analysis

Immunoblotting analysis was performed to analyse the microtubule-associated proteins 1A/1B light chain 3B (LC3B)-II/I and sequestosome-1 (SQSTM1) expression levels with anti-LC3B and anti-SQSTM1 antibodies, respectively, following the manufacturer's instructions (Table S3). The cells were plated in six-well plates and incubated with 400-μM FFA in the presence or absence of 3-μM VUTI for the indicated durations. Next, the cells were lysed with sodium dodecyl sulfate (SDS) lysis buffer supplemented with a protease inhibitor cocktail (Thermo Fisher Scientific, 78441). The proteins were subjected to immunoblotting. The intensity of each protein signal was normalized to that of actin beta (ACTB). The control value was set to 1.0, and the protein intensity was represented relative to that of the control.

To monitor the autophagy level, LC3B puncta in cells transfected with monomeric red fluorescent protein (mRFP)–green fluorescent protein (GFP) tandem fluorescence-tagged LC3B (tfLC3B) were examined using immunofluorescence microscopy. The cells cultured on glass coverslips were transfected with the mRFP–GFP tfLC3B plasmid. At 16 h after transfection, the cells were treated with 400-μM FFA and 3-μM VUTI in the presence or absence of bafilomycin A1 (InvivoGen, tlrl-baf1). Cellular localization of LC3B was observed using a Carl Zeiss Confocal LSM710 Meta microscope, and the images were processed and analysed using the software supplied by the manufacturer (Carl Zeiss, Seoul, Republic of Korea) and the NIH ImageJ software, respectively. Cells containing three or more mRFP–LC3B puncta were defined as autophagy-positive cells. The percentage of autophagy-positive cells relative to the total number of mRFP-positive cells was calculated. At least 100 mRFP-positive cells per sample were counted in at least three independent experiments. Cells stained with both red fluorescent protein (RFP) and GFP were defined as autophagosome-positive, while those stained with RFP only were defined as autolysosome-positive. The number of fluorescent LC3B puncta was determined by counting more than 100 cells in triplicate.

2.12 | Mitophagy activation analysis

Endogenous PRKN, PINK1, BNIP3L, LC3B and SQSTM1 expression levels were analysed using immunoblotting with the respective antibodies following the manufacturer's instructions (Table S3). The cells were plated into six-well plates and incubated with 125-μM PA in the presence or absence of 3-μM VUTI for 24 h. Next, the cells were lysed with SDS lysis buffer supplemented with a protease inhibitor cocktail (Thermo Fisher Scientific, 78441). Immunoblotting was performed as described above.

To monitor the mitophagy level, an mt-Keima-based mitophagy assay was performed using immunofluorescence microscopy. The cells expressing mt-Keima were plated onto a confocal dish, incubated with 125-μM PA in the presence or absence of 3-μM VUTI for 24 h and analysed using confocal microscopy. Mt-Keima protein was excited at 458 nm (neutral, pseudo-coloured in green) and 561 nm (acidic, pseudo-coloured in red) and detected through the same emission filter (570–695 nm). Laser power was set up at the lowest output to enable clear visualization of the mt-Keima signal and individualized for each experimental condition. Imaging settings were maintained with the same parameters for comparison between different experimental conditions. Additionally, images were acquired using a Carl Zeiss Confocal LSM710 Meta microscope (Carl Zeiss, Seoul, Republic of Korea). The fluorescence intensity was quantified using the NIH ImageJ software.

2.13 | Measurement of mitochondrial superoxide

Cells were plated in six-well plates and incubated with 125-μM palmitic acid in the presence or absence of 3-μM VUTI for 24 h. Next, the cells were pulsed with 2.5-μM MitoSOX Red mitochondrial superoxide indicator (Thermo Fisher Scientific, M36008) and 5-μM Hoechst 33342 (Thermo Fisher Scientific, H1399) for 30 min and subjected to live cell imaging at 37°C. After washing, the cells were observed under a confocal microscope in a chamber heated to 37°C at 5% CO$_2$. Images were acquired using a Carl Zeiss Confocal LSM710 Meta microscope (Carl Zeiss, Seoul, Republic of Korea). The fluorescence intensity was quantified using the NIH ImageJ software.

2.14 | Lipid peroxidation assay

Lipid peroxidation in the liver tissues and cells was determined by measuring the contents of malondialdehyde (MDA) resulting from the thiobarbituric acid reaction. The cells were plated in six-well plates and incubated with 125-μM PA in the presence or absence

of 3-μM VUTI for 24 h. Next, the cells were trypsinized and centrifuged. The cell pellets were washed with PBS and stored at −80°C until use. The MDA concentration was determined using the thiobarbituric acid reactive substance (TBARS) parameter assay kit (R&D Systems, KGE013) following the manufacturer's instructions.

To perform the 4-hydroxynonenal (4-HNE) assay, the cells were lysed using radioimmunoprecipitation assay (RIPA) buffer (Cell Signaling Technology) supplemented with a protease inhibitor cocktail (Thermo Fisher Scientific, 78441). The 4-HNE concentration was determined using the 4-HNE enzyme-linked immunosorbent assay (ELISA) kit (BioVision, E4645-100) following the manufacturer's instructions. All signal intensities in each experiment were normalized by the total protein concentration. The protein concentration was determined using the bicinchoninic acid (BCA) protein assay kit (Thermo Fisher Scientific, 23225).

2.15 | Measurement of the oxygen consumption rate (OCR)

OCR in human liver cells was measured using XFp Extracellular Flux Analyzers (Agilent Seahorse Biosciences). The cells were plated into XFp cell culture mini plates and incubated for 24 h. The culture medium was replaced with XF-Base medium (non-buffered Roswell Park Memorial Institute 1640 medium containing 2-mM L-glutamine, 1-mM sodium pyruvate and 10-mM glucose, pH 7.4) for 30 min. Next, the cells were incubated with VUTI (3 μM) for 15 min, followed by incubation with palmitic acid–BSA or BSA (control) of Seahorse XF Palmitate-BSA fatty acid oxidation (FAO) substrate (Agilent Seahorse Biosciences, 102720-100). Analysis was performed using the XF assay with Seahorse XF Long Chain Fatty Acid Oxidation Stress Test Kit (Agilent Seahorse Biosciences, 103672-100). Three measurements were assessed under basal conditions and after the addition of 2-μM oligomycin, 0.5-μM carbonyl cyanide-p-trifluoromethoxyphenylhydrazone (FCCP) and 1-μM rotenone/antimycin in the presence or absence of **etomoxir** (Etx; 4-μM final concentration). OCR values were normalized to the cell number.

2.16 | Intracellular localization of VUTI

Cells were cultured on glass coverslips and pulsed in the presence of propargylated VUTI (3 μM) for 5 h. After labelling, the cells were washed thrice with PBS and incubated in serum-free media with 100-nM MitoTracker Red (Invitrogen, M7512) for 30 min at 37°C in a 5% CO_2 incubator. The cells were then fixed with 4% paraformaldehyde in PBS for 10 min and stained with 10-μM Alexa Fluor 488 azide (Invitrogen, A10266) for 30 min using the Click-iT Cell Reaction Buffer Kit (Invitrogen, C10269) following the manufacturer's instructions. Next, the cells were washed thrice with PBS. The images were acquired using a Carl Zeiss Confocal LSM710 Meta microscope (Carl Zeiss, Seoul, Republic of Korea). The data were analysed using the NIH ImageJ software.

2.17 | Quantification of PON2 enzyme activity

2.17.1 | Intracellular PON2A activity in hepatocyte and liver tissues

Cells were plated into six-well plates and incubated with 125-μM palmitic acid in the presence or absence of 3-μM VUTI for 24 h. Next, the cells were trypsinized and centrifuged. The cell pellets were washed with PBS and stored at −80°C until use. The frozen cell pellets and liver tissues were incubated with 25-mM Tris buffer (pH 7.4) containing 0.05% n-dodecyl-β-D-maltoside (Merck, D4641) and 1-mM $CaCl_2$ and lysed by subjecting to three freeze–thaw cycles.

To evaluate the PON2 esterase activity, p-nitrophenyl acetate (pNPA) hydrolysis was determined using a SpectraMax Plus 384 Microplate Reader (Agilent Technologies, Seoul, Republic of Korea). The cell lysates were transferred to a 96-well plate, and reactions (0.2-ml final mixture volume) were initiated by adding 1-mM pNPA in PON2 activity assay buffer (50-mM Tris [pH 8.0] with 1-mM $CaCl_2$). The increase in absorbance at 412 nm resulting from the release of p-nitrophenol was monitored.

To evaluate the PON2 lactonase activity, the enzymatic hydrolysis of the thioalkyl-substituted lactones was determined. The cell and liver tissue lysates were transferred to a 96-well plate, and reactions were initiated by adding 1-mM 5-thiobutyl butyrolactone (TBBL) and 1-mM 5,5′-dithiobis(2-nitrobenzoic acid) (DTNB; Sigma-Aldrich, D8130) in PON2 activity assay buffer. The enzymatic hydrolysis was monitored by examining the absorbance of the reaction mixture at 420 nm.

All enzymatic activities in each experiment were normalized by the total protein concentration. The protein concentration was determined using the BCA protein assay kit (Thermo Fisher Scientific, 23225).

2.17.2 | Recombinant PON2 activity

To perform the oxidized linoleic acid (OX-LA)-mediated PON2 inhibition assay, purified recombinant PON2 protein (10 μM) was incubated with or without VUTI (10 μM) in the PON2 activity assay buffer in a 96-well plate for 10 min at room temperature. To inhibit PON2 activity, the samples were incubated with oxidized linoleic acid (100 μM) for 10 min at room temperature. To evaluate the esterase activity, the reactions were initiated by adding 1-mM pNPA to the PON2 activity assay buffer. The enzymatic hydrolysis was monitored by measuring the absorbance of the reaction mixture at 412 nm. To evaluate the lactonase activity, the reactions were initiated by adding 1-mM TBBL and 1-mM DTNB to the PON2 activity assay buffer. The enzymatic hydrolysis was monitored by measuring the absorbance of the reaction mixture at 420 nm.

2.18 | Chemical–protein interactome analysis to identify VUTI target proteins

2.18.1 | Preparation of protein samples

Biotin-conjugated VUTI was synthesized by incubating 20-μM propargylated VUTI with 10-μM biotin azide (Invitrogen, B10184) using the Click-iT Cell Reaction Buffer Kit (Invitrogen, C10269) for 30 min following the manufacturer's instructions. Biotin-conjugated VUTI was incubated with Dynabeads™ M-270 Streptavidin (Invitrogen, 65305) at 4°C for 1 h. The VUTI-bead complex was washed thrice with PBS. The cell lysates were incubated with the VUTI-bead complex at 4°C overnight. The beads were washed thrice with PBS, and the bound proteins were eluted with sodium dodecyl sulfate–polyacrylamide gel electrophoresis (SDS-PAGE) sample buffer and stored at −80°C until use.

2.18.2 | Interactome analysis of target proteins of VUTI

To identify VUTI-binding proteins, the bound proteins were digested. Briefly, the proteins were reduced in SDS lysis buffer (4% [w/v] SDS; 0.1-M Tris–HCl [pH 7.6]; 0.1-M dithiothreitol [DTT]) at 37°C for 45 min and boiled at 95°C for 10 min. The solution was concentrated using a 30 k membrane filter (Microcon devices, YM-30, Millipore, MA). The buffer was replaced with a 0.2-ml ursolic acid (UA) solution (8-M urea in 0.1-M Tris–HCl [pH 8.5]). The concentrates were mixed with 0.1 ml of 50-mM indole-3-acetic acid (IAA) in UA solution and incubated in the dark at room temperature for 30 min. The samples were centrifuged, washed with 0.2 ml of 50-mM tetraethylammonium bromide (TEAB) and centrifuged thrice at $14,000 \times g$ for 30 min. Next, 500 ng of trypsin prepared in 0.1 ml of 100-mM TEAB (with an enzyme-to-protein ratio of 1:50) was added to the filter, and the samples were incubated at 37°C overnight. The peptides were collected by centrifuging the filter units at $14,000 \times g$ for 30 min. TEAB (50 μl, 50 mM) was added to the filter, and the samples were centrifuged twice at $14,000 \times g$ for 20 min. Analytical (75 μm × 50 cm, C18, 3 μm, 100 Å) and trap columns (75 μm × 2 cm, C18, 3 μm, 100 Å) were used to separate the peptide samples. Solvents A and B were 0.1% formic acid in water and 0.1% formic acid in acetonitrile, respectively. The proteomic profile analysis conditions were as follows:- 2%–30% Solvent B for 60 min, 25%–90% Solvent B for 2 min, 90% Solvent B for 8 min and 2% Solvent B for 20 min. The eluted peptides from liquid chromatography (LC) were subjected to mass spectrometry using a Q Exactive HF-X Mass Spectrometer (Thermo Fisher Scientific, Bremen, Germany). Protein identification was performed using Proteome Discoverer 2.4 (Thermo Fisher Scientific) software and the UniProt Human (January 2021, 20,452 entries) database. Cellular components and biological processes in which each protein was enriched were analysed using Gene Ontology (GO) with g:Profiler.

2.19 | Evaluation of VUTI–PON2 interaction using the competitive binding assay

To confirm the interaction between VUTI and PON2, the VUTI-bead complex was prepared as described above and incubated with cell lysates at 4°C overnight. The beads were washed thrice with PBS, eluted with SDS-PAGE sample buffer and subjected to immunoblotting with the anti-PON2 antibodies.

To perform the competitive binding assay, cell lysates were incubated with free VUTI at the indicated concentrations (0–5 μM) for 5 h at 4°C. Next, the VUTI-bead complex was incubated with the free VUTI-treated cell lysates at 4°C overnight. The beads were washed thrice with PBS, and the bound proteins were eluted with SDS-PAGE sample buffer. The samples were then subjected to immunoblotting with anti-PON2 antibodies.

2.20 | Immunoblotting analysis

The Immuno-related procedures used comply with the recommendations made by the *British Journal of Pharmacology* (Alexander, Roberts et al., 2018). To extract proteins, the cultured cells and liver tissues were lysed using SDS lysis buffer (100-mM Tris–HCl, pH 6.8, 10% glycerol and 1% SDS) supplemented with a protease inhibitor cocktail (Thermo Fisher Scientific, 78441). The protein concentration was determined using the BCA protein assay kit (Thermo Fisher Scientific, 23225). The samples were boiled in $1\times$ sample buffer (10-mM Tris–HCl [pH 6.8], 1% SDS, 5% glycerol, 0.05% bromophenol blue and 1% β-mercaptoethanol) for 5 min and subjected to SDS-PAGE. To determine mitochondrial OXPHOS component levels, the samples were not boiled. The resolved proteins were electro-transferred to an Immobilon-P membrane (Merck, IPVH00010). The membrane was probed with specific antibodies listed in Table S3. Immunoreactive signals were detected using a LAS-4000 Luminescent Image Analyzer (GE Healthcare Bio-Sciences). The signal intensity was assessed by measuring the relative density of each band and normalizing the values to that of ACTB using the Multi Gauge software (Fujifilm).

2.21 | Data analysis and statistics

The data and statistical analysis comply with the recommendations of the *British Journal of Pharmacology* on experimental design and analysis in pharmacology (Curtis et al., 2022). Each study was designed to generate equal group sizes. Each experimental group within a series was assigned an integer, with all mice randomly assigned to these different experimental groups using a random number generator. We worked through the groups in the order assigned by the random number generator. All studies were also investigator-blinded with respect to treatment and during analysis. A different researcher made up the drugs for administration to blind the experimenter, and data analysis was performed by a researcher not directly involved in performing the
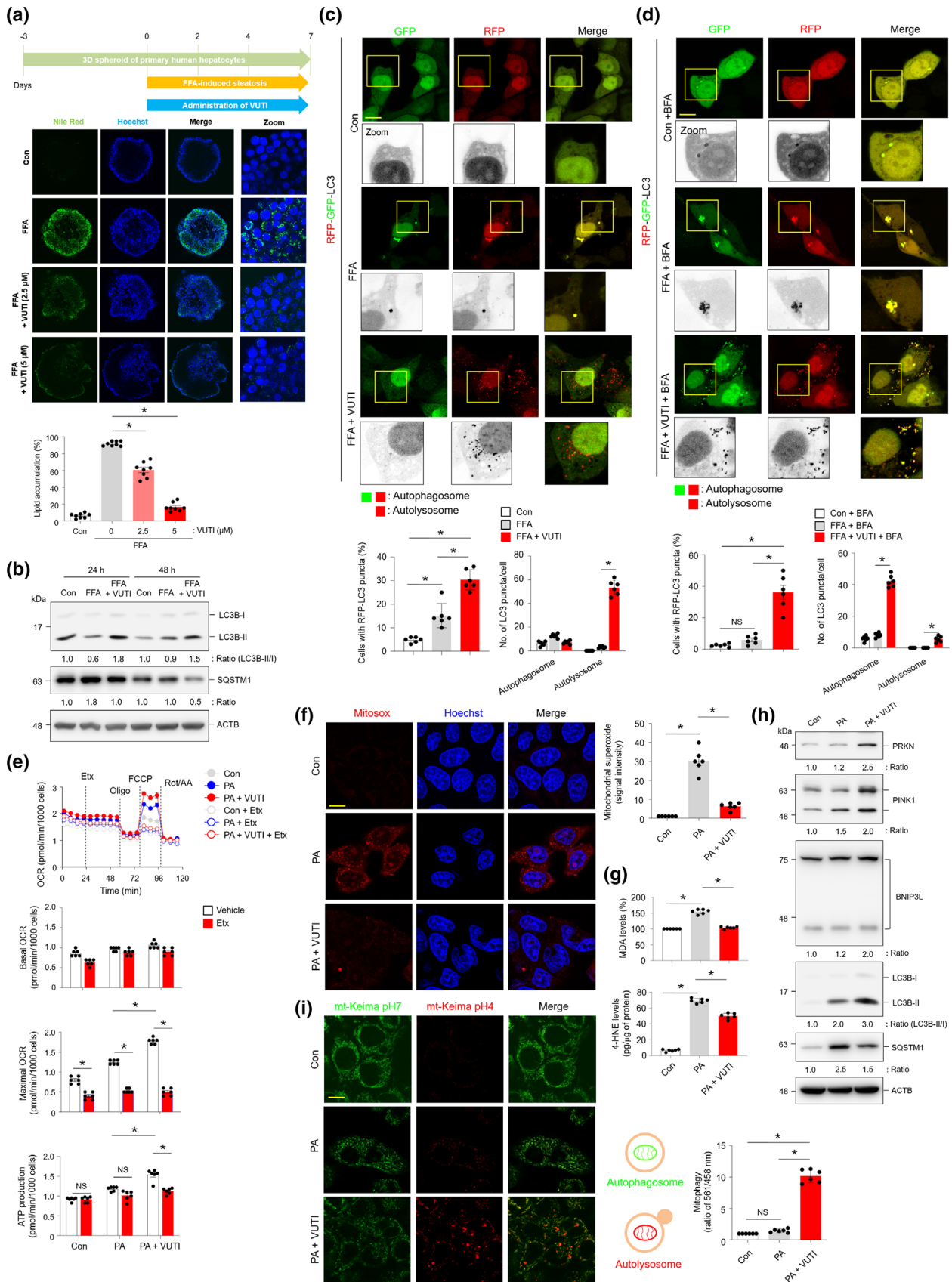
FIGURE 1 Legend on next page.

experiment. The justification of group sizes is based on published data and our previous experience.

All data, except RNA-sequencing (RNA-Seq) data, were expressed as the means ± standard error of the mean (SEM) and analysed with GraphPad Prism (Version 9 for Windows; GraphPad Software, Inc., San Diego, CA). Data were obtained from at least three independent experiments. Each group had at least n = 5, thus permitting statistical analysis. The declared group size is the number of independent values, and statistical analysis was done using these independent values. Statistical analyses were performed using analysis of variance (ANOVA) for multiple comparisons to determine the changes in body weight and food intake. Post hoc analysis was only conducted if F in the ANOVA achieved significance ($P < 0.05$). For comparisons between two groups, we used an unpaired, two-tailed Student's t test with Welch's correction. The changes in the histological scores before and after treatment were analysed using Fisher's exact test in comparison with the vehicle group. The Shapiro–Wilk test was used to test for a Gaussian distribution if the data were not normal. The F test was used to assess the assumption of equal variances. If variances were significantly different, a t test with Welch's correction and an ANOVA test were used. P values less than 0.05 were considered statistically significant.

2.22 | Materials

Synthetic glabridin derivatives (VUTI and HSG4113) and 5-thiobutyrolactone (TBBL) were prepared at Glaceum Inc. (Suwon, Republic of Korea) following the protocols mentioned in the patent US9783551B2 (Figure S1A) (Yu et al., 2017). The stock solution of synthetic glabridin derivatives were dissolved in dimethyl sulfoxide (DMSO) which was purchased from Sigma-Aldrich (St. Louis, MO, U.S. A). For the in vitro model study, DMSO is used as a control. For animal model studies, vehicle groups received the same volume of 0.9% normal saline.

Other compounds that were purchase from Sigma-Aldrich were isoflurane (792632), iodoacetamide (I6125), dibasic sodium phosphate (567547), BSA-conjugated oleic acid (OA, O300) and palmitic acid (P0500), Oil Red O solution (O1391), and 1-mM 5,5′-dithiobis(2-nitrobenzoic acid) (DTNB, D8130), dithiothreitol (DTT, D9776), triethylammonium bicarbonate (TEAB, 18597), formin acid (695076), trifluoroacetic aicd (91707), while enrofloxacin was purchased from Bayer (Leverkusen, Germany) and carprofen from Pfizer (NY, USA). Further, n-dodecyl-β-d-maltoside was obtained from Merck (Seoul, Republic of Korea).

Details of other materials and suppliers were provided in the specific sections.

2.23 | Nomenclature of targets and ligands

Key protein targets and ligands in this article are hyperlinked to corresponding entries in the IUPHAR/BPS Guide to PHARMACOLOGY http://www.guidetopharmacology.org and are permanently archived in the Concise Guide to PHARMACOLOGY 2023/24 (Alexander, Fabbro, et al., 2023; Alexander, Kelly, et al., 2023).

3 | RESULTS

3.1 | Vutiglabridin (VUTI) reduces lipid accumulation, activates autophagy and improves mitochondrial dysfunction in in vitro fatty liver model

To investigate the effect of VUTI in an in vitro fatty liver model, we first determined the optimal dose of VUTI. VUTI had less effect on cell toxicity up to 10 μM (Figure S1B). Then, we examined lipid accumulation in a 3D spheroid culture system of primary human hepatocyte. VUTI blocked FFA-induced lipid accumulation in the spheroids of primary human hepatocyte (Figure 1a). VUTI also reduced FFA-induced lipid accumulation in 2D culture systems of L02 hepatocytes (Figure S2A,B), indicating that VUTI acts to improve hepatic lipid accumulation.

Because autophagy is important for regulation of lipid metabolism, oxidative stress and inflammation (Xie et al., 2020), we investigated the effect of VUTI on autophagy activation. Immunoblotting analysis showed that VUTI increased the autophagic flux, as evidenced by the up-regulation of LC3B levels and the down-regulation

FIGURE 1 Beneficial effects of vutiglabridin (VUTI) the in vitro fatty liver model. (a) Lipid accumulation analysis in 3D spheroids of primary human hepatocyte (PHH) treated with FAs alone or in combination with VUTI, followed by staining with Nile Red (scale bar = 50 μm; n = 8). Cell nuclei were stained with Hoechst 33342. (b) Immunoblotting analysis of the autophagy flux (LC3B and SQSTM1) in L02 human hepatocytes. ACTB was used as a loading control. Confocal fluorescence analysis of the autophagy flux with (c) or without (d) bafilomycin A, an autophagy maturation inhibitor. L02 cells were transfected with the tandem fluorescent probe-tagged LC3B (mRFP–GFP–LC3B) plasmid. L02 cells with both red and green fluorescent puncta (autophagosome) and those with only red fluorescent puncta (autolysosome) were quantified (scale bar = 20 μm). (e) Mitochondrial oxygen consumption rate in L02 cells treated with etomoxir (Etx) following treatment with palmitic acid (PA) or its combination with VUTI. (f) Confocal fluorescence analysis of the generation of mitochondrial superoxide using MitoSOX staining (scale bar = 20 μm). (g) Quantification of lipid peroxidation in L02 cells treated with PA or its combination with VUTI. L02 cells were measured using malonaldehyde (MDA) accumulation and 4-hydroxynonenal (4-HNE) assays. (h) Immunoblotting analysis of mitophagy activation (PRKN, PINK1, BNIP3L, LC3B and SQSTM1) in L02 cells. (i) Confocal fluorescence analysis of the mitophagic flux in cells transfected with mt-Keima, a pH-dependent fluorescent mitophagy probe (scale bar = 20 μm). Green fluorescent filaments (pH 7.0) of mt-Keima indicate mitochondrial networks, while enlarged red fluorescence of mt-Keima (pH 4.0) indicates the mitophagy flux (fused with lysosome). NS, non-significant; * $P < 0.05$.
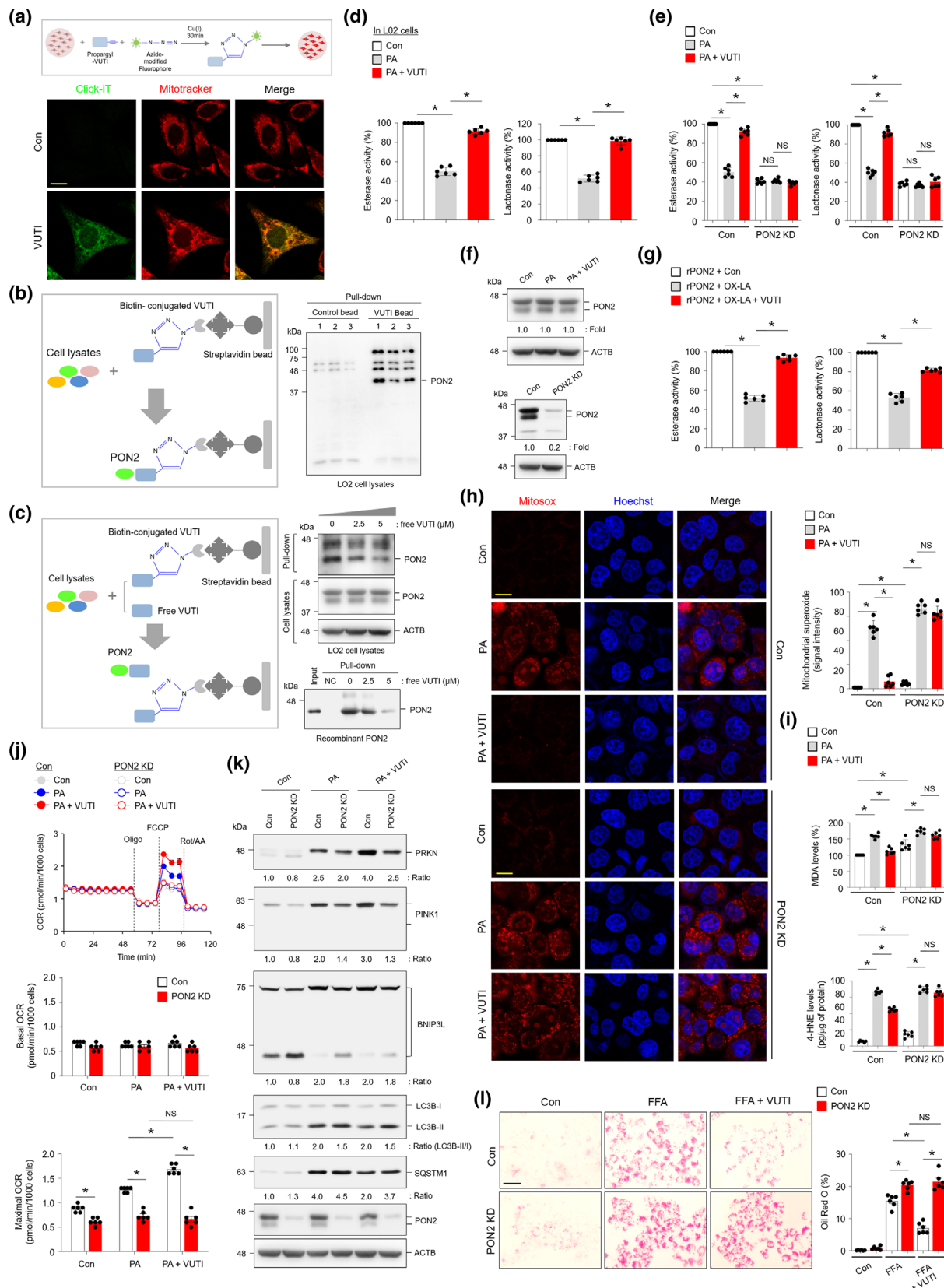
FIGURE 2 Legend on next page.

of SQSTM1 levels (Figure 1b). Confocal fluorescence analysis using the autophagy indicator tandem fluorescence-tagged LC3B plasmid revealed that VUTI promotes autolysosome maturation (Figure 1c). The number of VUTI-induced autolysosomes was reduced upon treatment with the lysosomal fusion inhibitor brefeldin A (BFA), whereas the number of autophagosomes was increased (Figure 1d). These results demonstrate that VUTI acts to activate autophagy flux.

To investigate the effect of VUTI on mitochondrial fatty acid (FA) oxidation (FAO) activation, the Seahorse XF palmitic acid–BSA. Fatty acid oxidation assay was performed using hepatocytes treated with etomoxir, which prevents the entry of FFA into mitochondria. The ATP production and maximal respiration capacity were higher in VUTI-treated cells than in control and palmitic acid-treated cells (Figure 1e). We then investigated the effect of VUTI on mitochondrial oxidative stress. VUTI down-regulated palmitic acid-induced mitochondrial superoxide levels to those observed in the control cells (Figure 1f). Additionally, VUTI down-regulated lipid peroxidation in the palmitic acid-treated hepatocytes (Figure 1g). Subsequently, we examined the effect of VUTI on mitophagy activation as a protective mechanism against cytotoxic reactive oxygen species (ROS) production by clearing damaged mitochondria. VUTI increased mitophagy activation by up-regulating PRKN/PINK1, BNIP3L and LC3B-II and down-regulating SQSTM1 (Figure 1h). Consistent with the results of the immunoblotting analysis, confocal fluorescence analysis using mt-Keima, a mitochondrial dual-excitation ratiometric fluorescent protein reporter of mitophagy, showed that VUTI increased the mitophagic flux, as evidenced by enhanced mitochondrial localization to the acidic lysosome (Figure 1i). These findings indicate that VUTI activates the autophagy– fatty acid oxidation axis and attenuates mitochondrial oxidative stress by activating mitophagy.

3.2 | PON2 is required for VUTI-induced promotion of autophagy activation and mitochondrial function

To investigate a major cellular target of VUTI, we examined the intracellular localization of VUTI using Alexa Fluor 488 azide-conjugated propargylated VUTI. Fluorescence analysis revealed that VUTI is primarily localized to the mitochondria (Figure 2a), indicating that VUTI acts to regulate mitochondrial function.

To identify the target proteins of VUTI, we performed the pull-down assay using biotin-labelled VUTI and cell lysates and analysed the chemical proteome. Based on the localization of VUTI, the enriched Gene Ontology terms for 130 VUTI-bound proteins in the mitochondria were related to the regulation of overall mitochondrial energy metabolism, including oxidative phosphorylation, fatty acid oxidation, tricarboxylic acid (TCA) cycle and oxidative stress homeostasis (Figure S3A,B). We identified PON2 as the target protein of VUTI (Figure 2b), because PON2 is primarily localized in mitochondria and is important for maintaining mitochondrial function, balancing lipid metabolism and mitigating inflammatory response (Ng et al., 2001; Shin et al., 2022). To confirm their selective interaction, a competitive pull-down assay was performed by pre-incubating the cell lysates with free VUTI. Free VUTI dose-dependently decreased the interaction between VUTI and PON2. This was consistent with the results of studies using purified recombinant PON2 protein (Figure 2c). Moreover, PON2 activity in VUTI-treated cells was examined to investigate the effect of the interaction between VUTI and PON2. These results indicate that PON2 is the cellular target protein of VUTI.

Because hepatic PON2 activity is inhibited by lipotoxic condition (Hussein et al., 2012), we investigated the effect of VUTI on the protection of PON2 activity under lipotoxic condition. Enzyme activity assay revealed that VUTI mitigates palmitic acid-induced inhibition of PON2 activity without affecting PON2 expression (Figure 2d,f). To confirm the specificity of the observed effect on PON2, the PON2 activity in PON2 KD cells was examined. VUTI did not improve palmitic acid-induced inhibition of PON2 activity in PON2 KD cells (Figure 2e,f). Additionally, VUTI inhibited oxidized linoleic acid-induced inhibition of purified PON2 activity (Figure 2g). These findings indicate that VUTI reactivates PON2 activity inhibited by toxic lipids.

To investigate the PON2 dependency of the beneficial effects of VUTI, we examined the effect of PON2 KD on mitochondrial superoxide production. VUTI down-regulated mitochondrial superoxide production in wild-type cells but not in PON2 KD cells (Figure 2h). Consistently, VUTI did not down-regulate lipid

FIGURE 2 Identification of paraoxonase-2 as a target protein of vutiglabridin (VUTI). (a) Confocal fluorescence analysis of the mitochondrial localization of VUTI in hepatocytes treated with Alexa Fluor 488 azide-conjugated propargylated VUTI. Mitochondria were stained with MitoTracker Red (scale bar = 20 μm). (b) Identification of paraoxonase-2 (PON2) as the target protein of VUTI using cell lysates and the propargylated VUTI–biotin–streptavidin bead complex, followed by immunoblotting. (c) Competitive binding assay to determine the specific interaction between VUTI and PON2. Cell lysates or purified recombinant PON2 protein was incubated with different concentrations of free VUTI, followed by incubation with streptavidin bead-conjugated VUTI. PON2 activities in hepatocytes (d) or PON2 knockdown (KD) cells (e) treated with palmitic acid (PA) alone or in combination with VUTI. (f) Immunoblotting analysis of PON2 expression in hepatocytes is shown in (d) and (e). (g) Purified recombinant PON2 activities following incubation with oxidized linoleic acid (OX-LA) alone or its combination with VUTI. (h) Confocal fluorescence analysis of the generation of mitochondrial superoxide in PON2 KD and control hepatocytes (scale bar = 20 μm). (i) Quantification of lipid peroxidation in PON2 KD and control hepatocytes. (j) Seahorse measurement of OCR in PON2 KD and control hepatocytes. (k) Immunoblotting analysis of mitophagy activation and flux (PRKN, PINK1, BNIP3L, LC3B and SQSTM1) in PON2 KD and control hepatocytes. (l) Lipid accumulation analysis in PON2 KD and control hepatocytes using Oil Red O staining (scale bar = 50 μm). *P < 0.05; NS, non-significant.
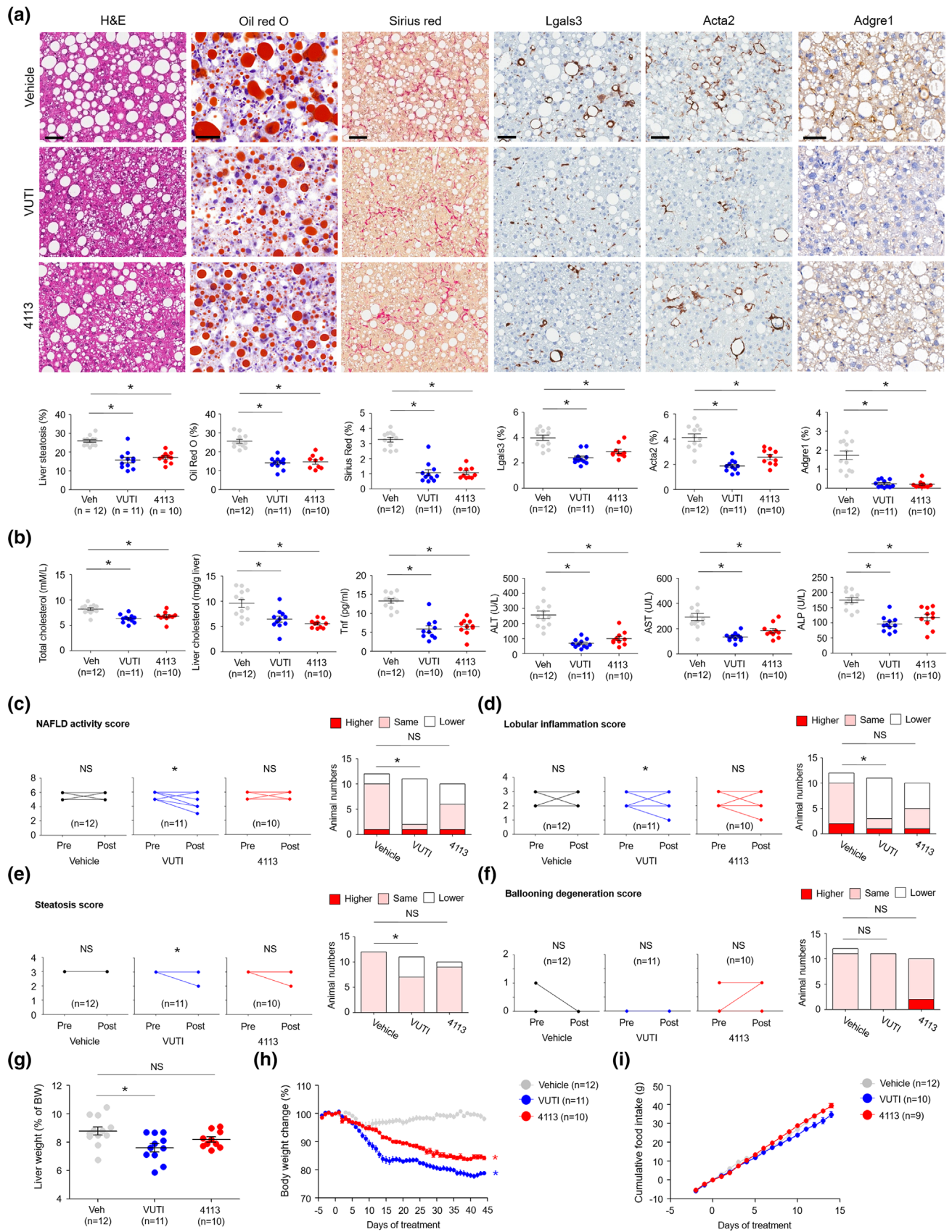
FIGURE 3 Legend on next page.

peroxidation in *PON2* KD cells (Figure 2i). Subsequently, we investigated the PON2 dependency of the effects of VUTI on fatty acid oxidation capacity. The promoting effect of VUTI on maximal respiration capacity was abolished in *PON2* KD cells (Figure 2j). *PON2* KD inhibited both VUTI-induced and basal autophagy/mitophagy activation (Figure 2k), as evidenced by SQSTM1 accumulation and PRKN and BNIP3L down-regulation. Finally, VUTI did not decrease lipid accumulation in *PON2* KD cells (Figure 2l). Altogether, these findings suggest that the beneficial effects of VUTI are dependent on PON2 activity.

3.3 | VUTI alleviates steatohepatitis in AMLN diet-induced NASH mouse model

The therapeutic efficacy of VUTI in progressive steatohepatitis was examined using an AMLN diet-induced obese (AMLN-DIO) NASH mouse model, which exhibits severe liver steatosis and inflammation. Mice with biopsy-confirmed NASH were administered synthetic glabridin derivatives during the last 6 weeks of AMLN diet supplementation (Figure S4A). VUTI and HSG4113 alleviated steatosis (haematoxylin and eosin [H&E] and Oil Red O staining), liver fibrosis (Sirius Red staining and Lgals3 and Acta2 immunostaining) and intrahepatic monocyte infiltration (Adgre1 immunostaining) (Figure 3a). Consistently, biochemical analyses revealed that VUTI and HSG4113 mitigated up-regulation of serum and hepatic cholesterol levels and plasma levels of fibroblast growth factor 21 (Fgf21) and leptin (steatosis markers), tumour necrosis factor-α (Tnf) and interleukin (Il)10 (inflammatory markers) and alanine aminotransferase (ALT), aspartate aminotransferase (AST) and alkaline phosphatase (ALP) (hepatic injury markers) but did not affect Il5, Il6 and chemokine ligand 1 (Cxcl1) levels (Figures 3b and S5A).

NASH-related phenotypes before VUTI treatment were compared with those at Week 6 after synthetic glabridin derivative treatment. Compared with that at baseline, the NASH activity score, which indicates the degree of lobular inflammation, steatosis and ballooning degeneration, was lower at week 6 after VUTI treatment. In contrast, the NASH activity score of the HSG4113 group did not differ at baseline and week 6 after treatment (Figures 3c–e and S6). Compared with that in the vehicle group, the number of mice exhibiting decreased NASH activity score was higher in the VUTI group and similar in the HSG4113 group. VUTI and HSG4113 did not alleviate hepatic ballooning and fibrosis (Figures 3f and S5B). Additionally, VUTI decreased liver and body weights (Figure 3g,h). The VUTI, HSG4113 and vehicle groups exhibited similar daily food intake (Figure 3i). These findings indicate that VUTI alleviated NASH with beneficial metabolic effects.

3.4 | VUTI was similarly efficacious to semaglutide in alleviating NASH features

Semaglutide, a glucagon-like peptide-1 receptor agonist, has been considered as a potential therapeutic for NASH and exhibited promising results in the clinical treatment of NASH in a recent phase 2 trial (Armstrong et al., 2016). Thus, we comparatively analysed the therapeutic effects of VUTI and semaglutide on NASH (Figure S4B). Similar to the anti-NASH effects of VUTI in short-term (6-week) treatment, long-term (10-week) treatment with VUTI alleviated hepatic steatosis in the AMLN-DIO NASH mouse model (Figure 4a) and down-regulated cholesterol levels (Figure 4b) to that observed in the semaglutide group. Semaglutide and VUTI mitigated liver fibrosis and intrahepatic monocyte infiltration (Figure 4a) and down-regulated Ccl2 (an inflammatory marker) and ALT, AST and ALP (hepatic injury markers) (Figure 4b).

The mice were stratified into VUTI, semaglutide and vehicle groups based on the NASH phenotypes at baseline. The NASH phenotypes at baseline were compared with those at week 10 after drug treatment. Treatment with VUTI and semaglutide for 10 weeks decreased the NASH activity score (Figure 4c). Additionally, the number of mice with decreased NASH activity score in the VUTI and semaglutide groups was higher than that in the vehicle group. In contrast to semaglutide, VUTI inhibited lobular inflammation (Figure 4d). However, VUTI and semaglutide did not prevent hepatic fibrosis (Figure S7A,B). VUTI and semaglutide decreased liver and body weights after treatment for 10 weeks (Figures 4e,f and S8A). The initial body weight reduction rate in the semaglutide group was higher than that in the VUTI group. However, the final body weight was similar in both groups (Figure 4f). Additionally, VUTI and semaglutide alleviated the AMLN diet-induced changes in body composition (Figure 4g,h) and adiposity (Figure S8B,C). In contrast to semaglutide, VUTI did not affect food intake (Figures 4i and S8D).

In addition to the therapeutic efficacy of VUTI in the AMLN-DIO NASH mouse model, the therapeutic efficacy of VUTI was also

---

FIGURE 3 Therapeutic effects of synthetic glabridin derivatives (SGDs) in an amylin diet-induced obese (AMLN-DIO) non-alcoholic steatohepatitis (NASH) mouse model. (a) Mice were fed with the AMLN diet, and NASH was confirmed using a biopsy. Next, the mice were orally administered VUTI and HSG4113 once daily for 6 weeks. Representative haematoxylin and eosin (H&E), Oil Red O and Sirius Red staining and Lgals3, Acta and Adgre1 immunostaining results (scale bar = 50 μm) and the histopathological scores. (b) Quantification of plasma total cholesterol, liver cholesterol and serum Tnf, alanine aminotransferase (ALT), aspartate aminotransferase (AST) and alkaline phosphatase (ALP). Histological scores of NAFLD activity (c), lobular inflammation (d), steatosis (e) and ballooning degeneration (f) in biopsies before (pre) and after treatment (post) are shown on the left. Numbers of animals exhibiting exacerbation (higher), no change (same) and alleviation (lower) of disease after treatment compared with conditions before treatment are shown on the right. Effect of SGDs on body weight (g), liver weight (h) and cumulative food intake (i). Data are presented as mean ± standard deviation (n = 12 for the vehicle group; n = 11 for the VUTI group; n = 10 for the HSG4113 group). *P < 0.05; NS, non-significant.

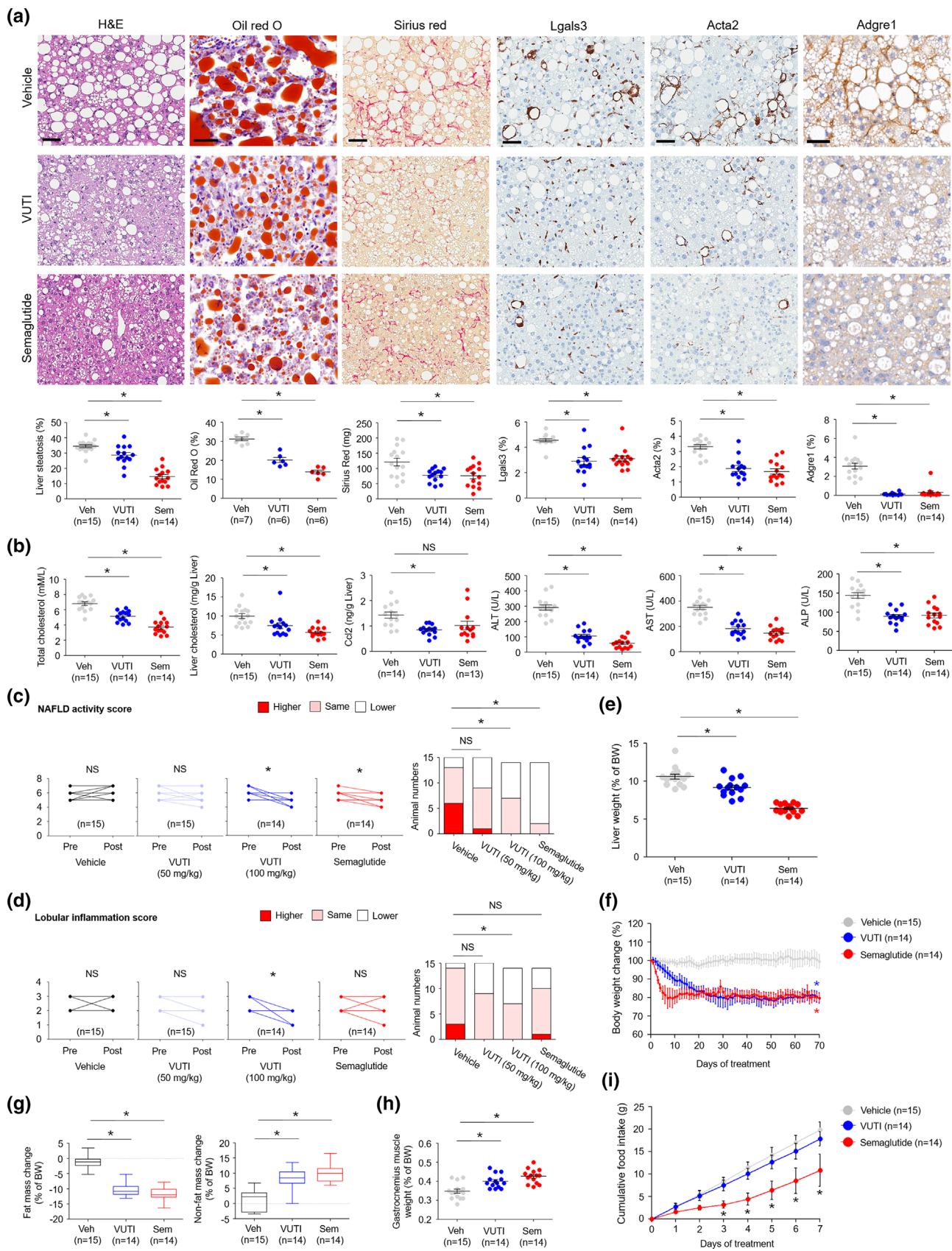**FIGURE 4** Legend on next page.

FIGURE 4 Distinct effects of vutiglabridin (VUTI) and semaglutide in an amylin diet-induced obese (AMLN-DIO) non-alcoholic steatohepatitis (NASH) mouse model. (a) AMLN-DIO NASH mice were treated once daily with VUTI and semaglutide for 10 weeks. Representative H&E, Oil Red O and Sirius Red staining and Lgals3, Acta2 and Adgre1 immunostaining (scale bar = 50 μm) results and the histopathological scores. (b) Quantification of plasma total cholesterol, liver cholesterol and liver CCL2 and serum ALT, AST and ALP. Histological scores of NAFLD activity (c) and lobular inflammation (d) in biopsies before (pre) and after treatment (post) are shown on the left. Numbers of animals exhibiting exacerbation (higher), no change (same) and alleviation (lower) of disease after treatment compared with conditions before treatment are shown on the right. Effects of VUTI and semaglutide on liver weight (e), body weight (f), fat/non-fat mass (g), muscle weight (h) and cumulative food intake (i). Data are presented as mean ± standard deviation (n = 15 for the vehicle group; n = 15 for the VUTI [50-mg·kg^{-1} body weight] group; n = 14 for the VUTI (100-mg·kg^{-1} body weight) group; n = 14 for the semaglutide group). *$P < 0.05$; NS, non-significant.

evaluated in the HF-DIO mouse model (Figure S9A). VUTI and semaglutide also reduced NASH activity score and liver and body weights in HF-DIO mouse model (Figure S9B,C). In accordance with these metabolic effects, VUTI and semaglutide reduced liver triglycerides, serum cholesterol, high-density lipoprotein and low-density lipoprotein (steatosis markers) and ALT (hepatic injury marker) (Figure S9D). These findings indicate that VUTI mitigates liver damage and improves NAFLD.

3.5 | VUTI treatment affects various hepatic lipid profiles in AMLN-DIO NASH mouse model

To investigate the mechanisms underlying the therapeutic effects of VUTI, the hepatic lipid profiles of the VUTI group were examined using LC–electrospray ionization–tandem mass spectrometry and compared with those of the semaglutide group. Principal component analysis revealed that the lipid profiles of the VUTI, semaglutide and vehicle groups exhibited distinct clustering (Figure 5a). Volcano plot analysis revealed that VUTI down-regulated 70 lipid species, including cholesterol esters (24:0 and 18:4) and triacylglycerols (42:2), while semaglutide down-regulated 128 lipid species, mainly triacylglycerols (42:2 and 44:4) (Figure 5b). VUTI up-regulated 37 lipid species, including sphingomyelins and phosphatidylcholines (PCs), while semaglutide up-regulated 31 lipid species, including phosphatidylcholines and FFAs. The relative contents and saturation levels of various glycerolipids were down-regulated in the VUTI and semaglutide groups (Figures 5c and S10). Additionally, VUTI down-regulated FFAs, ceramide and lysophospholipid (LPL) species, whereas semaglutide down-regulated phosphatidic acid.

The levels of 78 individual lipid species differed between the VUTI and semaglutide groups (Figures 5d and S11). VUTI down-regulated most individual monoacylglycerols, whereas semaglutide down-regulated most individual diacylglycerols and triacylglycerols. In contrast to semaglutide, VUTI down-regulated most individual lysophosphatidylcholines (LPCs), lysophosphatidylethanolamines (LPEs) and lysophosphatidylglycerols (LPGs) and up-regulated individual sphingomyelins. VUTI distinctively down-regulated some FAs, including long-chain FAs, whereas semaglutide up-regulated most FAs, including saturated and unsaturated FAs. The levels of cholesterol species and PCs were not different between the VUTI and semaglutide groups but were different from those in the vehicle group.

To identify lipid species that correlated with the alleviation of NASH, the levels of lipid species in the VUTI and semaglutide groups were comparatively analysed. A cluster of 10 lipid species, including phosphatidylethanolamine (PE), LPC, LPE, FFA and ceramide, positively correlated with NASH alleviation in the VUTI group. In the semaglutide group, eight lipid species, including phosphatidic acid and sphingomyelin, positively correlated with NASH alleviation (Figure 5e). LPC, LPE, FFA and ceramide levels positively correlated with the alleviation of hepatic inflammation in the VUTI group but not in the semaglutide group.

To examine the expression levels of lipid catabolic enzymes, the enrichment of differentially expressed genes (DEGs) in lipid metabolic pathways was calculated according to the Kyoto Encyclopedia of Genes and Genomes (KEGG) annotation. A schematic diagram of the lipid metabolic pathways revealed that FA uptake (*Slc27a*), TCA cycle (*Pdk1* and *Sdhd*), peroxisomal FA catabolism (*Acox1*, *Acox2*, *Acot4* and *Pecr*), mevalonate pathway (*Cyp51*, *Fdps*, *Nsdhl*, *Pmvk* and *Sqle*), ceramide biosynthesis from FAs (*Plpp3* and *Ugcg*) and lipolysis (*Fabp5* and *Lipc*) were enriched in both the VUTI and semaglutide groups (Figure 5f). The levels of genes related to peroxisomal FA uptake (*Abcd2* and *Abcd3*) and synthesis (*Acly*, *Acsl1* and *Acsl3*) were higher, whereas those of genes related to mitochondrial fatty acid oxidation (*Acaa2*, *Acadl*, *Echs1*, *Gcdh* and *Tpi1*), bile acid metabolism and secretion (*Cyp7b1*, *Akr1d1*, *Cyp27a1*, *Cyp39a1*, *Slco1a1*, *Slc10a1*, *Sult2a7*, *Ugt2b1*, *Ugt2b35* and *Adcy9*) and very-low-density lipoprotein (VLDL) biosynthesis from triacylglycerol (*Mttp*) were lower in the semaglutide group than in the VUTI group. In accordance with the lipidomic data (Figure 5c), the levels of *Agpat1* and *Agpat4*, encoding phospholipid (PL) (including palmitic acid, phosphatidylethanolamines (PE), phosphatidylcholines (PC), phosphatidylinositol [PI] and phosphatidylglycerol [PG]) biosynthesis enzymes from LPLs (including lysophosphatidic acid [LPA], LPE, LPC, LPI and LPG, respectively), were down-regulated in the semaglutide group but not in the VUTI group. These results demonstrate that VUTI promotes lipid catabolism to improve toxic lipid profiles.

3.6 | VUTI promotes autophagy activation and anti-inflammatory response in AMLN-DIO NASH mouse model

Transcriptomic analysis revealed the distinct mechanisms of NASH alleviation between VUTI and semaglutide. Of the 22,028 genes, the
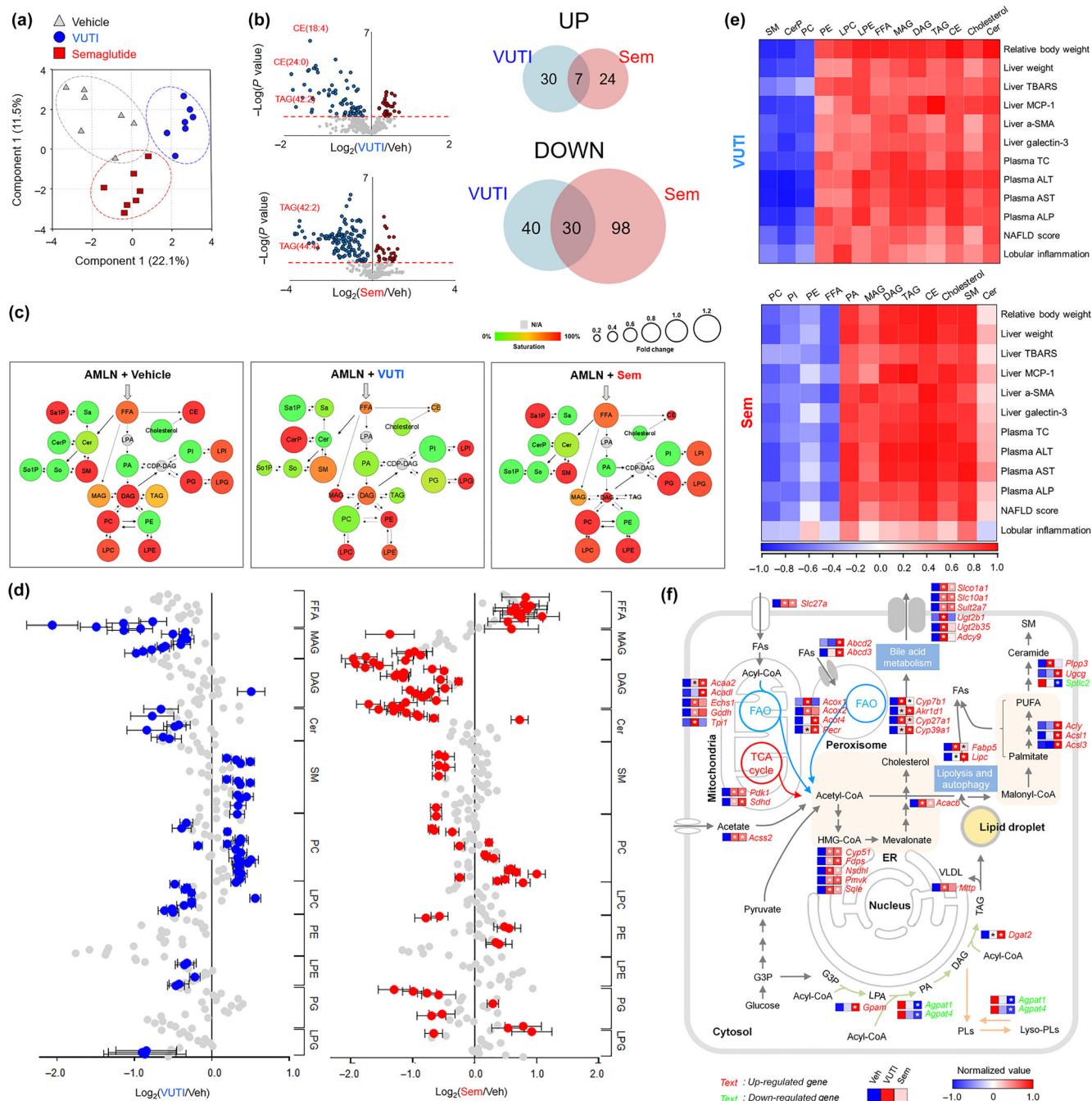
FIGURE 5 Lipidomic analysis in an amylin diet-induced obese (AMLN-DIO) non-alcoholic steatohepatitis (NASH) mouse model. (a) Principal coordinate analysis of hepatic levels of total lipids in the vehicle-, vutiglabridin (VUTI)- and semaglutide-treated AMLN-DIO NASH mice. (b) Volcano plot and Venn diagram analyses of the hepatic levels of total lipids in the VUTI and semaglutide groups compared with those in the vehicle group. (c) Analysis of hepatic lipid classes in the vehicle, VUTI and semaglutide groups. Lipid classes are presented as colour-coded circles. The percentage of saturated lipid species is shown for each class from green (low saturation) to red (high saturation). Unidentified lipid classes are shown in grey. The size of the circle is proportional to the fold change in the content of lipid species in the drug groups relative to the vehicle group (the arbitrary unit of 1). (d) Forest plots showing individual hepatic lipid species in the VUTI and semaglutide groups expressed as a fold change relative to the vehicle groups. Plots in blue or red represent differential individual lipid species between the drug and vehicle groups; $P < 0.05$. (e) Heatmap analysis of the correlation between lipid classes and pathological features in the VUTI and semaglutide groups. Each cell is colour-coded, and Pearson's correlation coefficient is shown. (f) Schematic representation of hepatic lipid metabolism showing genes that changed significantly in the VUTI and semaglutide groups compared with those in the vehicle group. Expression levels of genes are indicated by the heatmap. Each cell is colour-coded based on the relative abundance of genes in the drug groups relative to the vehicle group; $*P < 0.05$.
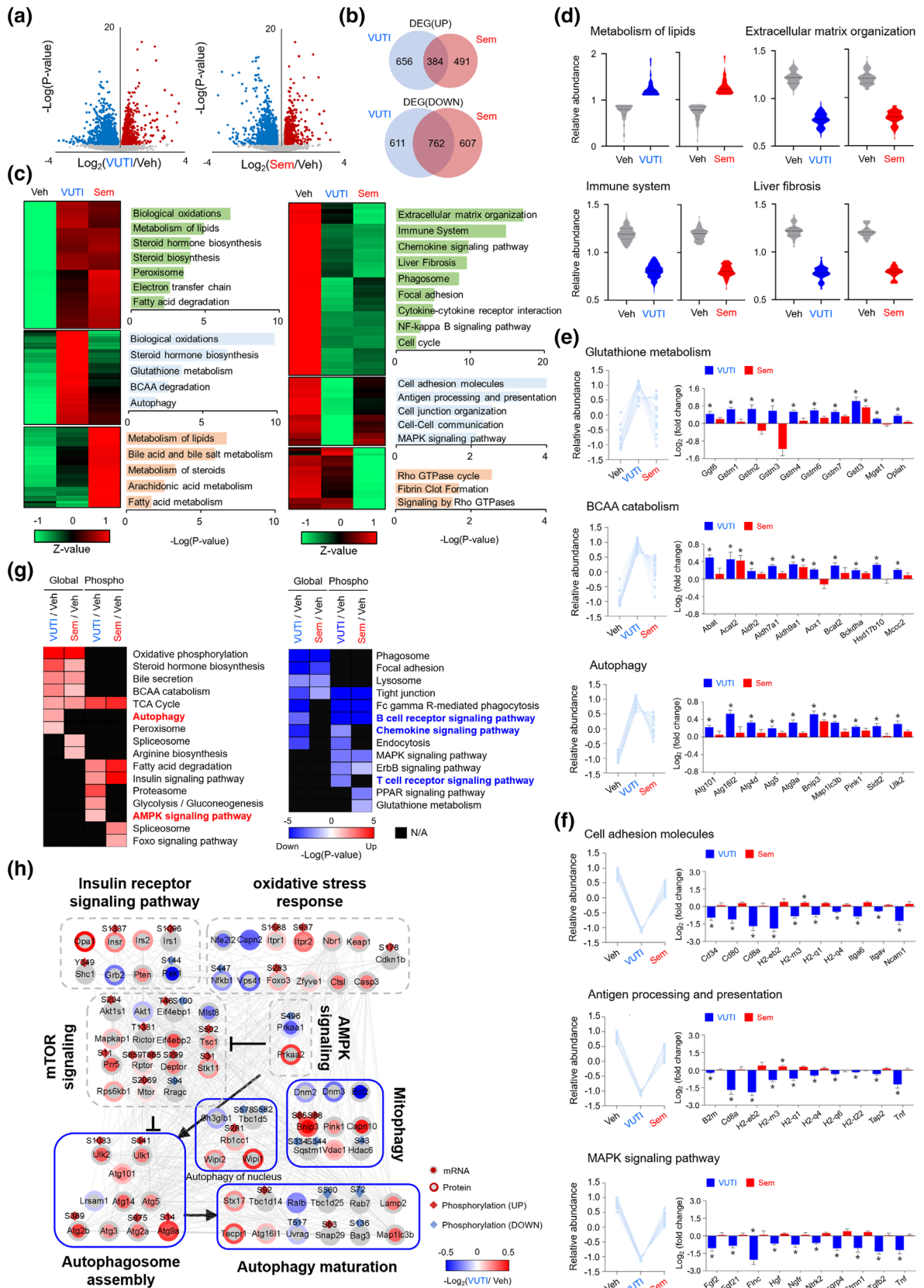
FIGURE 6   Legend on next page.

levels of approximately 10% of the genes in the semaglutide (2244 genes) and VUTI (2413 genes) groups were different from those in the vehicle group (Figure 6a). Among the meta-signature genes, VUTI and semaglutide co-regulated 1146 genes, which represent common gene signatures of the drugs for NASH alleviation (Figure 6b). Furthermore, VUTI and semaglutide altered the expression of 1267 and 1098 genes, respectively, which represent the drug-specific gene signatures. Gene Ontology analysis revealed that 384 up-regulated overlapping genes were enriched in biological oxidation, metabolism of lipids, steroid biosynthesis and FA degradation, whereas 762 down-regulated overlapping genes were enriched in the extracellular matrix organization, immune system, liver fibrosis and inflammation signalling (Figures 6c,d and S12). Meanwhile, 656 genes up-regulated in the VUTI group were related to glutathione metabolism, branched-chain amino acid degradation and autophagy, while 491 genes up-regulated in the semaglutide group were related to bile acid and arachidonic acid metabolism (Figure 6c,e). Furthermore, 611 genes down-regulated in the VUTI group were related to cell adhesion molecules, antigen processing and presentation, and mitogen-activated protein kinase (MAPK) signalling pathway, whereas 607 genes down-regulated in the semaglutide group were related to the Rho GTPase cycle and fibrin clot formation (Figure 6c,f).

Next, we comparatively analysed the phosphoproteome in the VUTI and semaglutide groups. Common signatures of up-regulated phosphoproteins and the corresponding total proteins were associated with oxidative phosphorylation, steroid hormone biosynthesis and FA degradation (Figure 6g). Meanwhile, common signatures of down-regulated phosphoproteins and the corresponding total proteins were associated with phagosomes, focal adhesion and tight junction. Phosphorylation of autophagy-linked Prkaa signalling pathway-related components was up-regulated, while phosphorylation of the B-cell receptor, chemokine and T-cell receptor signalling pathway-related components was down-regulated in the VUTI group compared with that in the semaglutide group.

We constructed functional interaction networks to examine the network of biological processes related to specific gene and protein signatures in the VUTI group (Figure 6h). Autophagy-linked biological processes were the major targets of VUTI: upstream of autophagy (insulin receptor signalling, oxidative stress response, mammalian target of rapamycin [Mtor] signalling and Prkaa signalling), autophagy initiation (Ulk1 and Ulk2), autophagosome biogenesis (Rb1cc1, Wipi1, Wipi2 and Atgs) and autophagy maturation (Map 1Lc3b, Stx17, Tecpr1 and Lamp2). These findings suggest that VUTI-induced autophagy activation is majorly important for alleviating NASH.

We validated the effect of VUTI on hepatic autophagy activation, mitochondrial function, inflammation and Pon2 activity in the liver of AMLN-DIO NASH mice. Map 1lc3b and Becn1 immunostaining analyses revealed that VUTI promoted autophagy activation in the mouse liver (Figure 7a). Immunoblotting analyses indicated that VUTI promoted activation of autophagy and lipid metabolism key regulator (Prkaa phosphorylation) and mitochondrial biogenesis (Ppargc1a levels) in the mouse liver (Figures S13A and 7b). VUTI increased the levels of hepatic mitochondrial DNA (mtDNA) contents and mitochondrial OXPHOS components except for Mtco1 expression in the mouse liver (Figures 7c and S13B). Consistent with reducing systemic inflammation (plasma Tnf levels) (Figure 3a,b) and mitigating macrophage infiltration (Adgre1 and Ccl2 levels in the liver) by VUTI treatment (Figure 4a,b), VUTI reduced hepatic inflammation (Il1b and Tnf levels) in the mouse liver (Figures 7d and S13C). Consistent with VUTI-mediated enhancing Pon2 activity in hepatocyte (Figure 2d), VUTI also increased Pon2 enzyme activity in the liver of AMLN-DIO NASH mice, whereas VUTI did not affect Pon2 protein levels (Figures 7e,f and S13D). VUTI down-regulated lipid peroxidation in the mouse liver (Figure 7g). Taken together with the effects of VUTI in an in vitro fatty liver model, these results indicated that the therapeutic effect of VUTI on alleviating NASH is closely associated with increasing PON2 activity, promoting autophagy activation, ameliorating mitochondrial dysfunction, reducing hepatic oxidative stress and mitigating hepatic inflammation in the mouse liver.

4 | DISCUSSION

Under lipid accumulation in the liver of NASH patients, the overloading of saturated fatty acids (FAs) into mitochondria promotes mitochondrial dysfunction through the accumulation of ROS in hepatocytes, exacerbating lipotoxicity and inflammation (Chen et al., 2018; Porcu et al., 2018). Thus, it has been considered that

FIGURE 6 Transcriptomic and phosphoproteomic analyses in an amylin diet-induced obese (AMLN-DIO) non-alcoholic steatohepatitis (NASH) mouse model. Volcano plot (a) and Venn diagram analysis (b) of hepatic differentially expressed genes (DEGs) between the vutiglabridin (VUTI)/semaglutide and vehicle groups. Genes up-regulated or down-regulated by more than twofold are shown in red and blue, respectively. (c) Two-dimensional hierarchical clustering shows the most significant Gene Ontology (GO) biological processes for each cluster of genes up-regulated (left panel) and down-regulated (right panel) in the VUTI and semaglutide groups (individually or in both groups) relative to the vehicle group. Red and green denote highly and weakly expressed genes, respectively. (d) Violin plots showing the mean and variance of overlapping gene clusters between the drug and vehicle groups. Among VUTI-specific gene clusters, the relative abundance scores of up-regulated (e) and down-regulated (f) genes were compared between all pairs of the VUTI, semaglutide and vehicle groups. (g) Top-ranked pathways in the phosphoproteomic analysis showing significantly up-regulated (red) or down-regulated (blue) phosphorylation (Phospho) and corresponding protein expressions (Global) in the VUTI and semaglutide groups relative to the vehicle group. (h) Network scheme showing the interactions of genes involved in the autophagy signalling pathway. The genes/proteins are selected from the DEGs of the transcriptomic and phosphoproteomic analyses with enhanced connectivity and significant differential expression in the VUTI group. Each gene/protein symbol is colour-coded based on the fold change. *P < 0.05. N/A, not available.
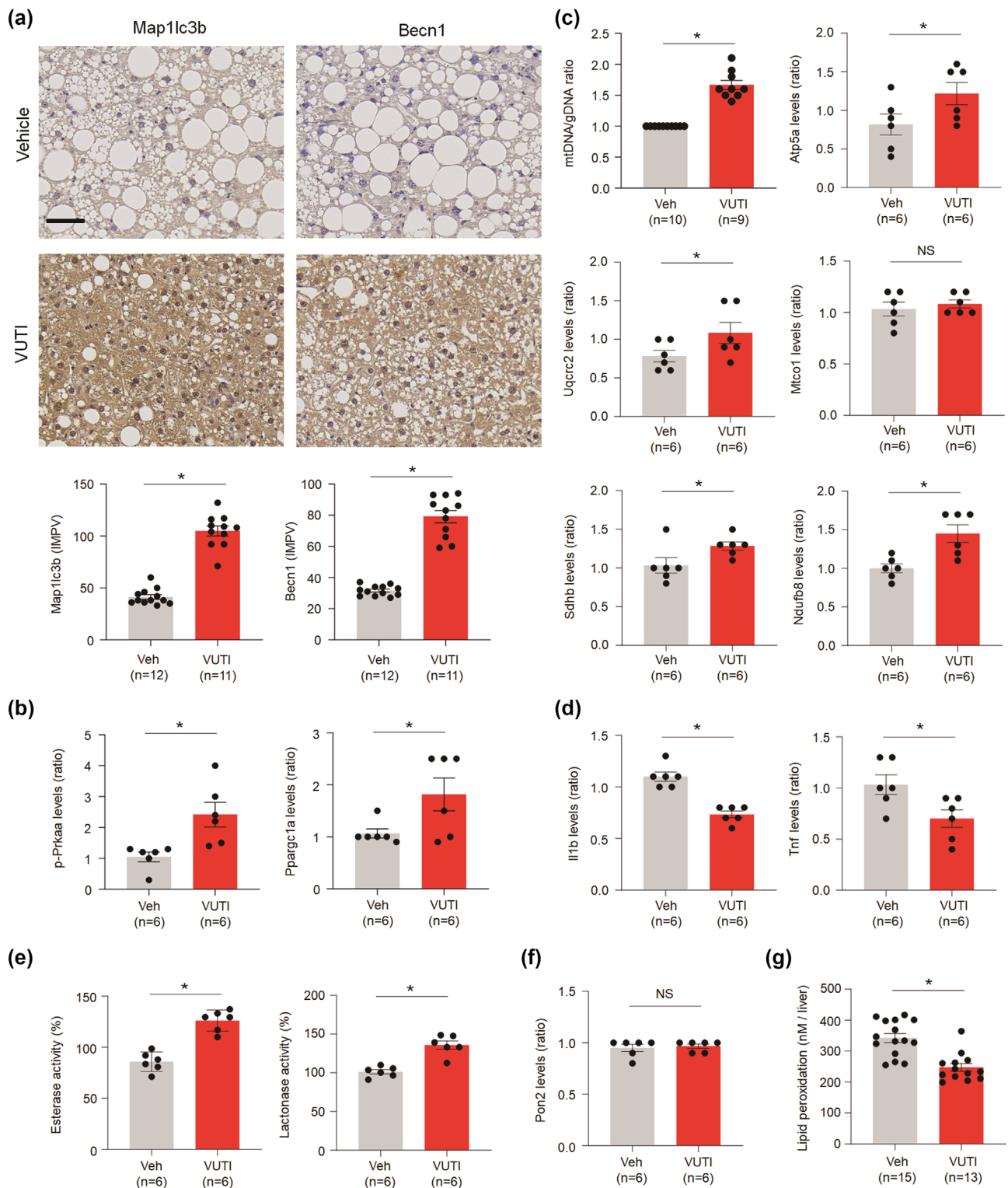
FIGURE 7 The effect of vutiglabridin (VUTI) on autophagy activation, mitochondrial function, inflammation and Pon2 enzyme activity in the mouse liver. (a) Immunohistochemical staining of Map 1lc3b and Becn1 levels in the livers of amylin diet-induced obese (AMLN-DIO) mice treated with the vehicle (n = 12) and VUTI (n = 11) (scale bar = 50 μm). IMPV, inverted mean pixel values. Quantification of Map 1lc3b and Becn1 protein levels was shown below. (b) Quantification of hepatic Prkaa activation and Ppargc1a expression in the livers of AMLN-DIO mice treated with the vehicle (n = 6) and VUTI (n = 6) that were validated by immunoblotting analysis. (c) Quantification of hepatic mitochondrial function containing mitochondrial DNA (mtDNA) contents and the levels of respiratory chain components in the livers of AMLN-DIO mice treated with the vehicle (n = 6) and VUTI (n = 6) that were validated by immunoblotting analysis. (d) Quantification of hepatic inflammation (Il1b and Tnf levels) in the livers of AMLN-DIO mice treated with the vehicle (n = 6) and VUTI (n = 6) that were validated by immunoblotting analysis. (e) Quantification of hepatic PON2 enzyme activity (esterase and lactonase activity) in the livers of AMLN-DIO mice treated with the vehicle (n = 6) and VUTI (n = 6). (f) Quantification of Pon2 expression in the livers of AMLN-DIO mice is shown in (e). (g) Quantification of hepatic lipid peroxidation in the livers of AMLN-DIO mice administered with VUTI (n = 13) and the vehicle (n = 15). *$P < 0.05$; NS, non-significant. [Correction added on 5 July 2024, after first online publication: Figure 7 has been updated in this version.]

promoting lipid catabolism, reducing oxidative stress and improving mitochondrial dysfunction in the liver are critically important for alleviating NASH. In this study, VUTI acts by decreasing oxidative stress, lipid peroxidation and mitochondrial dysfunction as well as reducing lipid accumulation in *in vitro* fatty liver models, suggesting that VUTI may be a fundamental therapeutic in NASH. We also evaluated the therapeutic effect of VUTI on NASH using a clinically relevant biopsy-confirmed NASH mouse model. VUTI exerted a prominent anti-inflammatory activity and mitigated the AMLN diet-induced adverse effects on the overall physical attributes, including body weight loss, liver weight loss and enhanced lean mass. Furthermore, VUTI improved hepatic steatosis and inflammation in the HF-DIO model. Our data indicated that VUTI reverses all aspects of NASH.

Autophagy contributes to promoting lipid catabolism by breaking down lipid droplets (Amir et al., 2013; Wang et al., 2010) and is thus important for the maintenance of overall liver homeostasis (Yan et al., 2017). In particular, mitophagy clears damaged mitochondria and promotes mitochondrial biosynthesis, thus maintaining mitochondrial homeostasis (Sidarala et al., 2020; Villa et al., 2018; Yang et al., 2014). Additionally, mitophagy alleviates mitochondrial oxidative stress (Sidarala et al., 2020; Yang et al., 2014). Metabolic disorders are characterized by markedly decreased autophagy activity, which leads to enhanced lipid accumulation, mitochondrial dysfunction, oxidative stress and inflammation (Perrotta & Aquila, 2015; Zhang et al., 2015). In NAFLD, the saturated FA-mediated suppression of autophagy activation exacerbates lipotoxicity and liver damage (Shin et al., 2022; Zhang et al., 2015). Thus, autophagy/mitophagy pathway activation has been considered a possible therapeutic target in NAFLD. Our omics data showed that VUTI promotes the activation of the autophagy pathway, including autophagy initiation, autophagosome formation and autolysosome maturation process in the AMLN-DIO NASH mouse model. In *in vitro* phenotypic results, VUTI restored palmitic acid-induced inhibition of autophagy/mitophagy activation in hepatocytes. Therefore, VUTI-mediated autophagy/mitophagy activation is important for the reversing all of NASH features.

Identification of the drug targets is essential to understanding the mechanism of action and determining the clinical dose regimen based on the drug-target engagement. The chemical–protein interactome demonstrated that PON2 is a specific target protein of VUTI. PON2 is expressed in most tissues, including the liver (Camps et al., 2009; Mochizuki et al., 1998). PON2 has been associated with NAFLD in clinical studies as well as preclinical models (Hussein et al., 2012; Kotani et al., 2021; Shin et al., 2022). In NAFLD models, PON2 activity is down-regulated through oxidative inactivation in the livers of the NAFLD rat model and in the *in vitro* fatty liver model (Boshtam et al., 2013; Hussein et al., 2012; Shin et al., 2022). In the present study, our data also showed that palmitic acid and oxidized linoleic acid inhibit PON2 activity in hepatocytes. A study using the *PON2* KD mouse model reported that PON2 deficiency decreases energy expenditure and oxidative capacity (Shih et al., 2019). Thus, reduced PON2 activity has been considered a risk factor for NAFLD. Additionally, PON2 is localized to intracellular regions, especially in the mitochondria and endoplasmic reticulum (ER), which are major sites for controlling oxidative stress and metabolism (Manco et al., 2021). PON2 deficiency promotes mitochondrial dysfunction, increases oxidative stress and augments inflammatory response in the liver and hepatocytes (Devarajan et al., 2011; Shin et al., 2022). Thus, enhancing PON2 activity may promote mitochondrial function and reduce oxidative stress, suggesting that PON2 agonist is a potential therapeutic for NASH. In the present study, VUTI promoted PON2 activity without affecting its expression. Additionally, VUTI-induced promotion of fatty acid oxidation and antioxidant capacity was dependent on PON2 activity. Indeed, VUTI-induced autophagy/mitophagy activation was diminished in *PON2* KD cells, leading to lipid accumulation. In addition, VUTI-induced PON2 activation reprogrammed the hepatic transcriptome and proteome associated with lipid catabolism, mitochondrial homeostasis, redox balance, inflammation and autophagy activation. Our data showed that VUTI-induced PON2 activation is important for regulating various functional pathways related to reversing NASH. Future research may include an in-depth study of the potential function of PON2 on transcriptional and post-translational regulation of various genes in endoplasmic reticulum (ER) and mitochondria.

The occurrence of NASH is associated with major abnormalities in hepatic lipid metabolism (Puri et al., 2007). Marked alterations in the hepatic lipidome are associated with the progression of NASH (Puri et al., 2007). In particular, NASH is correlated with the down-regulation of plasma phosphatidylserine (PS), phosphatidylethanolamine (PE), phosphatidylinositol (PI), phosphatidylcholines (PC) and sphingomyelin contents and the up-regulation of lysophospholipids (LPLs; Tiwari-Heckler et al., 2018). The accumulation of lysophosphatidylcholines (LPC), an important mediator of hepatic lipotoxicity, disrupts mitochondrial integrity and promotes the release of pro-inflammatory molecules (Hirsova et al., 2016; Hollie et al., 2014). Patients with NASH are characterized by increased levels of saturated FAs and decreased levels of polyunsaturated FAs (Allard et al., 2008). The balance between unsaturated and saturated FAs is important in alleviating hepatic lipotoxicity (López-Vicario et al., 2014). Thus, lipidomic profile analysis can aid in evaluating the therapeutic efficacy of drugs against NASH. In this study, the levels of individual lipid species in the lipidome differed between the VUTI and vehicle groups. VUTI up-regulated sphingomyelin and PC species and reduced the levels of the majority of LPLs and FA species compared with the vehicle. These findings indicate that VUTI improves hepatic function by altering the levels of particular lipid species in the hepatic lipidome. A previous study revealed that PON2 can affect the expression of various genes related to hepatic lipid metabolism (Shin et al., 2022). In this regard, VUTI-induced PON2 activation causes the alteration of particular lipid species by regulating gene expression related to lipid metabolism. Of note, PON2 can directly hydrolyse polyunsaturated FAs such as **arachidonic acid** and **docosahexaenoic acid** (Draganov et al., 2005). Thus, VUTI-induced PON2 activation may cause specific hydrolysis of individual FAs, leading to specific FA profiles, and this should be studied in the future. Taken together, VUTI, as a PON2 agonist, restores liver metabolic and lipidomic imbalance in NASH. It is unknown

whether such activity affects the regulation of metabolism in other tissues.

5 | CONCLUSIONS

In summary, our findings indicate that the NASH-alleviating effects of VUTI are dependent on PON2 activity that promotes autophagy/mitophagy activation and mitochondrial functions. Along with its advantage as an orally administered small molecule, VUTI is a promising therapeutic for NASH and protects hepatocytes. Furthermore, targeting PON2 may be important for improving liver function in various immune-metabolic diseases including NAFLD.

AUTHOR CONTRIBUTIONS

Gu-Choul Shin: Conceptualization (equal); data curation (equal); funding acquisition (equal); methodology (equal); project administration (equal); resources (equal); writing—original draft (equal); writing—review and editing (equal). **Hyeong Min Lee:** Conceptualization (equal); data curation (equal); formal analysis (equal); investigation (equal); methodology (equal); validation (equal). **Nayeon Kim:** Data curation (supporting); investigation (supporting); methodology (supporting). **Jihyeon Hur:** Data curation (supporting); investigation (supporting); methodology (supporting). **Sang-Ku Yoo:** Data curation (supporting); formal analysis (supporting); methodology (supporting). **Yun Sun Park:** Data curation (supporting); formal analysis (supporting). **Hyung Soon Park:** Data curation (supporting); methodology (supporting). **Dongryeol Ryu:** Data curation (supporting); methodology (supporting). **Min-Ho Park:** Investigation (supporting); methodology (supporting). **Jung Hee Park:** Investigation; methodology. **Sang-Uk Seo:** Investigation (supporting); methodology (supporting). **Leo Sungwong Choi:** Investigation (supporting); methodology (supporting). **Martin Rønn Madsen:** Methodology (supporting). **Michael Feigh:** Methodology (supporting). **Kwang Pyo Kim:** Funding acquisition (equal); supervision (equal); writing—review and editing (equal). **Kyun-Hwan Kim:** Funding acquisition (equal); supervision (equal); writing—review and editing (equal).

CONFLICT OF INTEREST STATEMENT

HML, S-KY, YSP and HSP are current employees of Glaceum Inc. and hold its stocks/shares. Glaceum Inc. holds the intellectual property rights of the synthetic glabridin derivatives. The remaining authors declare no competing interests.

DATA AVAILABILITY STATEMENT

All data supporting the findings of this study are available within the article and its supporting information and from the corresponding author upon reasonable request. The RNA-Seq datasets used in this study are publicly available and can be found in the GEO database (https://www.ncbi.nlm.nih.gov/geo/) (accession number: GSE222659). The raw LC–MS/MS data are available at www.proteomexchange.org under the Dataset Identifier Numbers PXD039524 and PXD03952.

DECLARATION OF TRANSPARENCY AND SCIENTIFIC RIGOUR

This Declaration acknowledges that this paper adheres to the principles for transparent reporting and scientific rigour of preclinical research as stated in the *BJP* guidelines for Design & Analysis, Immunoblotting and Immunochemistry and Animal Experimentation and as recommended by funding agencies, publishers and other organizations engaged with supporting research.

ORCID

Gu-Choul Shin 🔟 https://orcid.org/0000-0001-8200-9700
Min-Ho Park 🔟 https://orcid.org/0000-0002-5927-6701
Leo Sungwong Choi 🔟 https://orcid.org/0000-0001-8850-0832

REFERENCES

Ahn, J., Lee, H., Jang, J., Kim, S., & Ha, T. (2013). Anti-obesity effects of glabridin-rich supercritical carbon dioxide extract of licorice in high-fat-fed obese mice. *Food and Chemical Toxicology*, *51*, 439–445. https://doi.org/10.1016/j.fct.2012.08.048

Alexander, S. P. H., Fabbro, D., Kelly, E., Mathie, A. A., Peters, J. A., Veale, E. L., Armstrong, J. F., Faccenda, E., Harding, S. D., Davies, J. A., Annett, S., Boison, D., Burns, K. E., Dessauer, C., Gertsch, J., Helsby, N. A., Izzo, A. A., Ostrom, R., Papapetropoulos, A., … Wong, S. S. (2023). The Concise Guide to PHARMACOLOGY 2023/24: Enzymes. *British Journal of Pharmacology*, *180*, S289–S373. https://doi.org/10.1111/bph.16181

Alexander, S. P. H., Kelly, E., Mathie, A. A., Peters, J. A., Veale, E. L., Armstrong, J. F., Buneman, O. P., Faccenda, E., Harding, S. D., Spedding, M., Cidlowski, J. A., Fabbro, D., Davenport, A. P., Striessnig, J., Davies, J. A., Ahlers-Dannen, K. E., Alqinyah, M., Arumugam, T. V., Bodle, C., … Zolghadri, Y. (2023). The Concise Guide to PHARMACOLOGY 2023/24: Introduction and Other Protein Targets. *British Journal of Pharmacology*, *180*, S1–S22. https://doi.org/10.1111/bph.16176

Alexander, S. P. H., Roberts, R. E., Broughton, B. R. S., Sobey, C. G., George, C. H., Stanford, S. C., Cirino, G., Docherty, J. R., Giembycz, M. A., Hoyer, D., Insel, P. A., Izzo, A. A., Ji, Y., MacEwan, D. J., Mangum, J., Wonnacott, S., & Ahluwalia, A. (2018). Goals and practicalities of immunoblotting and immunohistochemistry: A guide for submission to the British Journal of Pharmacology. *British Journal of Pharmacology*, *175*, 407–411. https://doi.org/10.1111/bph.14112

Allard, J. P., Aghdassi, E., Mohammed, S., Raman, M., Avand, G., Arendt, B. M., Jalali, P., Kandasamy, T., Prayitno, N., Sherman, M., Guindi, M., Ma, D. W. L., & Heathcote, J. E. (2008). Nutritional assessment and hepatic fatty acid composition in non-alcoholic fatty liver disease (NAFLD): A cross-sectional study. *Journal of Hepatology*, *48*, 300–307. https://doi.org/10.1016/j.jhep.2007.09.009

Amir, M., Zhao, E., Fontana, L., Rosenberg, H., Tanaka, K., Gao, G., & Czaja, M. J. (2013). Inhibition of hepatocyte autophagy increases tumor necrosis factor-dependent liver injury by promoting caspase-8 activation. *Cell Death and Differentiation*, *20*, 878–887. https://doi.org/10.1038/cdd.2013.21

Ao, M., Shi, Y., Cui, Y., Guo, W., Wang, J., & Yu, L. (2010). Factors influencing glabridin stability. *Natural Product Communications*, *5*, 1907–1912. https://doi.org/10.1177/1934578X1000501214

Armstrong, M. J., Gaunt, P., Aithal, G. P., Barton, D., Hull, D., Parker, R., Hazlehurst, J. M., Guo, K., Abouda, G., Aldersley, M. A., Stocken, D., Gough, S. C., Tomlinson, J. W., Brown, R. M., Hübscher, S. G., & Newsome, P. N. (2016). Liraglutide safety and efficacy in patients with non-alcoholic steatohepatitis (LEAN): A multicentre, double-blind, randomized, placebo-controlled phase 2 study. *Lancet*, *387*, 679–690. https://doi.org/10.1016/S0140-6736(15)00803-X

Bae, I. Y., Choi, M. S., Ji, Y. S., Yoo, S. K., Kim, K., & Yoo, H. H. (2020). Species differences in stereoselective pharmacokinetics of HSG4112, a new anti-obesity agent. *Pharmaceutics.*, *12*, 127. https://doi.org/10.3390/pharmaceutics12020127

Baker, P. R., & Friedman, J. E. (2018). Mitochondrial role in the neonatal predisposition to developing nonalcoholic fatty liver disease. *The Journal of Clinical Investigation*, *128*, 3692–3703. https://doi.org/10.1172/JCI120846

Barb, D., Portillo-Sanchez, P., & Cusi, K. (2016). Pharmacological management of nonalcoholic fatty liver disease. *Metabolism*, *65*, 1183–1195. https://doi.org/10.1016/j.metabol.2016.04.004

Belinky, P. A., Aviram, M., Fuhrman, B., Rosenblat, M., & Vaya, J. (1998). The antioxidative effects of the isoflavan glabridin on endogenous constituents of LDL during its oxidation. *Atherosclerosis*, *137*, 49–61. https://doi.org/10.1016/S0021-9150(97)00251-7

Boshtam, M., Emami Razavi, A., Pourfarzam, M., Ani, M., Naderi, G. A., Basati, G., Mansourian, M., Dinani, N. J., Asgary, S., & Abdi, S. (2013). Serum paraoxonase 1 activity is associated with fatty acid composition of high density lipoprotein. *Disease Markers*, *35*, 273–280. https://doi.org/10.1155/2013/612035

Camps, J., Marsillach, J., & Joven, J. (2009). The paraoxonases: Role in human diseases and methodological difficulties in measurement. *Critical Reviews in Clinical Laboratory Sciences*, *46*, 83–106. https://doi.org/10.1080/10408360802610878

Chen, X., Yi, L., Song, S., Wang, L., Liang, Q., Wang, Y., Wu, Y., & Gao, Q. (2018). Puerarin attenuates palmitate-induced mitochondrial dysfunction, impaired mitophagy and inflammation in L6 myotubes. *Life Sciences*, *206*, 84–92. https://doi.org/10.1016/j.lfs.2018.05.041

Curtis, M. J., Alexander, S. P. H., Cirino, G., George, C. H., Kendall, D. A., Insel, P. A., Izzo, A. A., Ji, Y., Panettieri, R. A., Patel, H. H., Sobey, C. G., Stanford, S. C., Stanley, P., Stefanska, B., Stephens, G. J., Teixeira, M. M., Vergnolle, N., & Ahluwalia, A. (2022). Planning experiments: Updated guidance on experimental design and analysis and their reporting III. *British Journal of Pharmacology*, *179*, 3907–3913. https://doi.org/10.1111/bph.15868

Devarajan, A., Bourquard, N., Hama, S., Navab, M., Grijalva, V. R., Morvardi, S., Clarke, C. F., Vergnes, L., Reue, K., Teiber, J. F., & Reddy, S. T. (2011). Paraoxonase 2 deficiency alters mitochondrial function and exacerbates the development of atherosclerosis. *Antioxidants & Redox Signaling*, *14*, 341–351. https://doi.org/10.1089/ars.2010.3430

Draganov, D. I., Teiber, J. F., Speelman, A., Osawa, Y., Sunahara, R., & La Du, B. N. (2005). Human paraoxonases (PON1, PON2, and PON3) are lactonases with overlapping and distinct substrate specificities. *Journal of Lipid Research*, *46*, 1239–1247. https://doi.org/10.1194/jlr.M400511-JLR200

Haas, J., Francque, S., & Staels, B. (2016). Pathophysiology and mechanisms of nonalcoholic fatty liver disease. *Annual Review of Physiology*, *78*, 181–205. https://doi.org/10.1146/annurev-physiol-021115-105331

Hirsova, P., Ibrahim, S. H., Krishnan, A., Verma, V. K., Bronk, S. F., Werneburg, N. W., Shah, V. H., Malhi, H., Gores, G. J., & Gores, G. J. (2016). Lipid-induced signaling causes release of inflammatory extracellular vesicles from hepatocytes. *Gastroenterology*, *150*, 956–967. https://doi.org/10.1053/j.gastro.2015.12.037

Hollie, N. I., Cash, J. G., Matlib, M. A., Wortman, M., Basford, J. E., Abplanalp, W., & Hui, D. Y. (2014). Micromolar changes in lysophosphatidylcholine concentration cause minor effects on mitochondrial permeability but major alterations in function. *Biochimica et Biophysica Acta*, *1841*, 888–895. https://doi.org/10.1016/j.bbalip.2013.11.013

Hussein, O., Zidan, J., Abu Jabal, K., Shams, I., Szvalb, S., Grozovski, M., Bersudsky, I., Karry, R., & Aviram, M. (2012). Paraoxonase activity and expression is modulated by therapeutics in experimental rat nonalcoholic fatty liver disease. *International Journal of Hepatology*, *2012*, 265305.

Ito, C., Oi, N., Hashimoto, T., Nakabayashi, H., Aoki, F., Tominaga, Y., Yokota, S., Hosoe, K., & Kanazawa, K. (2007). Absorption of dietary licorice isoflavan glabridin to blood circulation in rats. *Journal of Nutritional Science and Vitaminology (Tokyo)*, *53*, 358–365. https://doi.org/10.3177/jnsv.53.358

Kotani, K., Watanabe, J., Miura, K., & Gugliucci, A. (2021). Paraoxonase 1 and non-alcoholic fatty liver disease: A meta-analysis. *Molecules*, *26*, 2323. https://doi.org/10.3390/molecules26082323

Lilley, E., Stanford, S. C., Kendall, D. E., Alexander, S. P. H., Cirino, G., Docherty, J. R., George, C. H., Insel, P. A., Izzo, A. A., Ji, Y., Panettieri, R. A., Sobey, C. G., Stefanska, B., Stephens, G., Teixeira, M., & Ahluwalia, A. (2020). ARRIVE 2.0 and the British Journal of Pharmacology: Updated guidance for 2020. *British Journal of Pharmacology*, *177*, 3611–3616. https://doi.org/10.1111/bph.15178

López-Vicario, C., González-Périz, A., Rius, B., Morán-Salvador, E., García-Alonso, V., Lozano, J. J., Bataller, R., Cofán, M., Kang, J. X., Arroyo, V., Clària, J., & Titos, E. (2014). Molecular interplay between Δ5/Δ6 desaturases and long-chain fatty acids in the pathogenesis of non-alcoholic steatohepatitis. *Gut*, *63*, 344–355. https://doi.org/10.1136/gutjnl-2012-303179

Manco, G., Porzio, E., & Carusone, T. (2021). Human paraoxonase-2 (PON2): Protein functions and modulation. *Antioxidants (Basel)*, *10*, 256. https://doi.org/10.3390/antiox10020256

Mochizuki, H., Scherer, S. W., Xi, T., Nickle, D. C., Majer, M., Huizenga, J. J., Tsui, L. C., & Prochazka, M. (1998). Human *PON2* gene at 7q21.3: Cloning, multiple mRNA forms, and missense polymorphisms in the coding sequence. *Gene*, *13*, 149–157. https://doi.org/10.1016/S0378-1119(98)00193-0

Ng, C. J., Wadleigh, D. J., Gangopadhyay, A., Hama, S., Grijalva, V. R., Navab, M., Fogelman, A. M., & Reddy, S. T. (2001). Paraoxonase-2 is a ubiquitously expressed protein with antioxidant properties and is capable of preventing cell-mediated oxidative modification of low density lipoprotein. *The Journal of Biological Chemistry*, *276*, 44444–44449. https://doi.org/10.1074/jbc.M105660200

Percie du Sert, N., Hurst, V., Ahluwalia, A., Alam, S., Avey, M. T., Baker, M., Browne, W. J., Clark, A., Cuthill, I. C., Dirnagl, U., Emerson, M., Garner, P., Holgate, S. T., Howells, D. W., Karp, N. A., Lazic, S. E., Lidster, K., MacCallum, C. J., Macleod, M., … Würbel, H. (2020). The ARRIVE guidelines 2.0: Updated guidelines for reporting animal research. *British Journal of Pharmacology*, *177*, 3617–3624. https://doi.org/10.1111/bph.15193

Perrotta, I., & Aquila, S. (2015). The role of oxidative stress and autophagy in atherosclerosis. *Oxidative Medicine and Cellular Longevity*, *2015*, 130315. https://doi.org/10.1155/2015/130315

Porcu, C., Sideri, S., Martini, M., Cocomazzi, A., Galli, A., Tarantino, G., & Balsano, C. (2018). Oleuropein induces AMPK-dependent autophagy in NAFLD mice, regardless of the gender. *International Journal of Molecular Sciences*, *19*, 3948. https://doi.org/10.3390/ijms19123948

Puri, P., Baillie, R. A., Wiest, M. M., Mirshahi, F., Choudhury, J., Cheung, O., Sargeant, C., Contos, M. J., & Sanyal, A. J. (2007). A lipidomic analysis of nonalcoholic fatty liver disease. *Hepatology*, *46*, 1081–1090. https://doi.org/10.1002/hep.21763

Shih, D. M., Meng, Y., Sallam, T., Vergnes, L., Shu, M. L., Reue, K., Tontonoz, P., Fogelman, A., Lusis, A., & Reddy, S. (2019). PON2 deficiency leads to increased susceptibility to diet-induced obesity. *Antioxidants*, *8*, 19. https://doi.org/10.3390/antiox8010019

Shin, G. C., Lee, H. M., Kim, N., Yoo, S. K., Park, H. S., Choi, L. S., Kim, K. P., Lee, A. R., Seo, S. U., & Kim, K. H. (2022). Paraoxonase-2 contributes to promoting lipid metabolism and mitochondrial function via autophagy activation. *Scientific Reports*, *12*, 21483. https://doi.org/10.1038/s41598-022-25802-1

Sidarala, V., Pearson, G. L., Parekh, V. S., Thompson, B., Christen, L., Gingerich, M. A., Zhu, J., Stromer, T., Ren, J., Reck, E. C., Chai, B., Corbett, J. A., Mandrup-Poulsen, T., Satin, L. S., & Soleimanpour, S. A. (2020). Mitophagy protects β cells from inflammatory damage in diabetes. *JCI Insight*, *5*, e141138. https://doi.org/10.1172/jci.insight.141138

Tiwari-Heckler, S., Gan-Schreier, H., Stremmel, W., Chamulitrat, W., & Pathil, A. (2018). Circulating phospholipid patterns in NAFLD patients associated with a combination of metabolic risk factors. *Nutrients*, *10*, 649. https://doi.org/10.3390/nu10050649

Villa, E., Marchetti, S., & Ricci, J. (2018). No parkin zone: Mitophagy without parkin. *Trends in Cell Biology*, *28*, 882–895. https://doi.org/10.1016/j.tcb.2018.07.004

Wang, Y., Singh, R., Xiang, T., & Czaja, M. J. (2010). Macroautophagy and chaperone-mediated autophagy are required for hepatocyte resistance to oxidant stress. *Hepatology*, *52*, 266–277. https://doi.org/10.1002/hep.23645

Wu, F., Jin, Z., & Jin, J. (2013). Hypoglycemic effects of glabridin, a polyphenolic flavonoid from licorice, in an animal model of diabetes mellitus. *Molecular Medicine Reports*, *7*, 1278–1282. https://doi.org/10.3892/mmr.2013.1330

Xie, Y., Li, J., Kang, R., & Tang, D. (2020). Interplay between lipid metabolism and autophagy. *Frontiers in Cell and Development Biology*, *8*, 431. https://doi.org/10.3389/fcell.2020.00431

Yan, S., Huda, N., Khambu, B., & Yin, X. M. (2017). Relevance of autophagy to fatty liver diseases and potential therapeutic applications. *Amino Acids*, *49*, 1965–1979. https://doi.org/10.1007/s00726-017-2429-y

Yang, S., Xia, C., Li, S., Du, L., Zhang, L., & Zhou, R. S. (2014). Defective mitophagy driven by dysregulation of rheb and KIF5B contributes to mitochondrial reactive oxygen species (ROS)-induced nod-like receptor 3 (NLRP3) dependent proinflammatory response and aggravates lipotoxicity. *Redox Biology*, *3*, 63–71. https://doi.org/10.1016/j.redox.2014.04.001

Yehuda, I., Madar, Z., Leikin-Frenkel, A., & Tamir, S. (2015). Glabridin, an isoflavan from licorice root, downregulates iNOS expression and activity under high-glucose stress and inflammation. *Molecular Nutrition & Food Research*, *59*, 1041–1052. https://doi.org/10.1002/mnfr.201400876

Yu, S. K., Suk, K. K., Young, K. J., Wook, C. J., Ho, I. J., & Yoo, J. I. G. (2017). Pyranochromenyl phenol derivative, and pharmaceutical composition for treating metabolic syndrome or inflammatory disease—Patent US9783551B2—PubChem.

Zhang, Q., Li, Y., Liang, T., Lu, X., Zhang, C., Liu, X., Jiang, X., Martin, R. C., Cheng, M., & Cai, L. (2015). ER stress and autophagy dysfunction contribute to fatty liver in diabetic mice. *International Journal of Biological Sciences*, *11*, 559–568. https://doi.org/10.7150/ijbs.10690

SUPPORTING INFORMATION

Additional supporting information can be found online in the Supporting Information section at the end of this article.